The ASC inflammasome adapter controls the extent of peripheral protein aggregate deposition in inflammation-associated amyloidosis

Marco Losa[1], Marc Emmenegger[1], Pierre De Rossi[2,#], Patrick M Schürch[3,#], Tetiana Serdiuk[4,#], Niccolò Pengo[5], Danaëlle Capron[5], Dimitri Bieli[5], Niels J Rupp[6,7], Manfredi C Carta[1], Karl J Frontzek[1], Veronika Lysenko[3], Regina R Reimann[1], Asvin KK Lakkaraju[1], Mario Nuvolone[1,8], Gunilla T Westermark[9], K. Peter R. Nilsson[10], Magdalini Polymenidou[2], Alexandre P. A. Theocharides[3], Simone Hornemann[1], Paola Picotti[4], and Adriano Aguzzi[1,†]

[1] Institute of Neuropathology, University of Zurich, Zurich, Switzerland

[2] Department of Quantitative Biomedicine, University of Zürich, Zurich, Switzerland

[3] Department of Medical Oncology and Hematology, University Hospital Zurich, Zurich, Switzerland

[4] Institute of Molecular Systems Biology, Department of Biology, ETH Zurich, Zurich, Switzerland

[5] Mabylon AG, Schlieren, Zurich, Switzerland

[6] Department of Pathology and Molecular Pathology, University Hospital Zurich, Zurich, Switzerland

[7] Faculty of Medicine, University of Zurich, Zurich, Switzerland

[8] Amyloidosis Research and Treatment Center, Fondazione Instituto di Ricovero e Cura a Carattere Scientifico (IRCCS) Policlinico San Matteo, University of Pavia, Pavia, Italy

[9] Department of Medical Cell Biology, Uppsala University, Uppsala, Sweden

[10] Department of Physics, Chemistry and Biology, Linköping University, Linköping, Sweden

[#] Equal contribution

[†]Corresponding author: Adriano Aguzzi, Institute of Neuropathology, University of Zurich Schmelzbergstrasse 12, CH-8091 Zurich, Switzerland, E-mail: adriano.aguzzi@usz.ch

Abstract

ASC-containing inflammasomes form specks, extracellular aggregates which enhance the aggregation of Aβ amyloid in Alzheimer's disease. This raises the question whether ASC participates to additional aggregation proteinopathies. Here we show that ASC controls the extent of inflammation-associated AA amyloidosis, a systemic disease caused by the aggregation of the acute-phase reactant serum amyloid A (SAA). Using superresolution microscopy, we found that ASC colocalized tightly with SAA in human AA amyloidosis. Purified recombinant ASC specks accelerated SAA fibril formation *in vitro*. Mass spectrometry after limited proteolysis showed that ASC interacts with SAA via its pyrin domain. In a murine model of inflammation-associated AA amyloidosis, splenic AA amyloid load was conspicuously decreased in *Pycard*$^{tm1Vmd/tm1Vmd}$ mice which lack ASC. This reduction was not a consequence of enhanced amyloid phagocytosis, as SAA stimulation increased phagocytic activity in *Pycard*$^{+/+}$, but not in *Pycard*$^{-/-}$ macrophages. Treatment with anti-ASC antibodies decreased the amyloid loads in wild-type mice suffering from AA amyloidosis. The prevalence of natural anti-ASC IgG ($-\log EC_{50} \geq 2$) in 19,334 hospital patients was <0.01%, suggesting that anti-ASC antibody treatment modalities would not be confounded by natural autoimmunity. Higher anti-ASC titers did not correlate with any specific disease, suggesting that anti-ASC immunotherapy may be well-tolerated. These findings expand the role played by ASC to extraneural proteinopathies of humans and experimental animals and suggest that anti-ASC immunotherapy may contribute to resolving such diseases.

43 **Introduction**

44 Inflammation-associated amyloid A (AA) amyloidosis occurs in a heterogeneous spectrum of chronic
45 conditions including inflammatory bowel disease, tuberculosis, hepatitis, genetic inflammatory
46 diseases (e.g., familial Mediterranean fever), cancer as well as autoimmune diseases such as
47 rheumatoid arthritis and vasculitis [1-3]. In these conditions, cytokines stimulate hepatocytes to
48 synthesize and secrete Serum Amyloid A (SAA) into the bloodstream. During the acute-phase response,
49 serum SAA can increase 1000-fold from its baseline concentration [4, 5]. Persistently high levels of SAA in
50 serum can hamper its proper processing and clearance, leading to nucleation of aggregated AA fibrils
51 and systemic deposition of AA amyloid. The deposition of amyloid in spleen, kidney, liver, and heart
52 can be massive and cause life-threatening disruption of tissue integrity [6-8].

53 There is increasing evidence for an important role of innate immunity in the pathogenesis of protein
54 misfolding diseases (PMDs) [9-13]. The adapter protein ASC (Apoptosis-associated speck-like protein
55 containing a caspase recruitment domain) plays an eminent role in the pathogenesis of Alzheimer's
56 disease (AD) [14-16]. Intrahippocampal injection of microglia-derived ASC specks leads to amyloid β (Aβ)
57 cross-seeding in mice overexpressing Amyloid-β Precursor Protein and Presenilin-1 (APP/PS1;*Pycard*$^{+/+}$
58 mice) which is reduced in APP/PS1;*Pycard*$^{-/-}$ mice. This increase in Aβ pathology can be prevented by
59 co-injection of ASC specks with anti-ASC antibodies [15, 17].

60 Aβ and AA amyloid consist of β-pleated sheets and have similar fibril sizes, fibril strand orientations,
61 and cross-seeding capability [18]. Indirect evidence suggests a role for ASC in the pathogenesis of
62 inflammation-associated (AA) amyloidosis. ASC was shown to colocalize with AA amyloid in kidney
63 biopsies from patients with AA amyloidosis secondary to familial Mediterranean fever, where a gain-
64 of-function mutation in the *Pyrin* gene activates ASC inflammasomes and leads to chronic
65 overexpression of SAA [19]. Also, cryopyrin-associated periodic syndrome (CAPS) patients, owing to a
66 genetic condition, have constitutively high NLRP3 and ASC inflammasome activation [20, 21] and are at
67 high risk of developing AA amyloidosis [2]. SAA activates the NLRP3 inflammasome of human myeloid
68 cells via an interaction with the P2X7 receptor, which induces ASC release *in vitro* through a cathepsin

69 B-sensitive pathway [22]. Additionally, the SAA cascade may prompt the upregulation of pro-
70 inflammatory cytokines and enhances fibrillogenic activity towards SAA1 *in vitro* in murine
71 macrophages [23, 24].
72 In a murine model of AA amyloidosis, subcutaneous administration of silver nitrate ($AgNO_3$), coupled
73 with an intravenous application of preformed SAA fibrils (known as Amyloid Enhancing Factor or AEF),
74 rapidly induces AA amyloidosis in spleen [25-27]. $AgNO_3$ serves as a proinflammatory stimulus that leads
75 to elevation in SAA serum levels, while preformed AA fibrils (AEF) serve as a template for SAA
76 aggregation [28]. Interestingly, depletion of splenic macrophages delays or inhibits AA amyloid
77 accumulation in mice [25, 29] and macrophages can clear AA amyloid via Fc-receptor-mediated
78 phagocytosis [30]. These results suggest that components of the innate immune system may control,
79 both positively and negatively, the course of AA amyloidosis.
80 Here, we investigated the role of ASC in inflammation-associated amyloidosis *in vitro* and *in vivo.* We
81 found that ASC forms complexes with SAA in post-mortem tissue of a patient with inflammation-
82 associated AA amyloidosis, colocalizes with murine splenic AA amyloid, accelerates SAA fibril formation
83 and interacts with SAA via its pyrin domain. *Pycard*$^{+/+}$ mice exhibited progressive splenic amyloidosis
84 and a concomitant decrease in SAA serum concentration, both of which were attenuated in the
85 absence of ASC. Treatment with anti-ASC antibodies decreased amyloid loads and improved health in
86 a mouse model of amyloidosis, suggesting that anti-ASC immunotherapy may be useful in this
87 condition.

88 **Results**

89 ***Colocalization of ASC with amyloid A***

90 As ASC colocalizes with Aβ amyloid in mice and humans [15], we asked whether ASC would colocalize
91 also with AA, a type of extraneural amyloid composed of SAA fibrils. We used the amyloidotropic dye
92 Congo Red (CR) and antibodies against ASC to stain cardiac tissues from a patient suffering from
93 vasculitis and systemic inflammation-associated AA amyloidosis and, for control, a 68-year-old male
94 patient without any clinical sign of amyloidosis who died from left ventricular failure after myocardial
95 infarction (**Fig. 1A**). CR-stained amyloidotic tissue, but not control tissue, showed a characteristic red
96 appearance (**Fig. 1B**). ASC immunoreactivity was predominantly intramuscular and vascular, and
97 appeared more pronounced in the amyloidosis patient. We then probed the potential colocalization
98 between ASC and SAA using antibodies against ASC, SAA, and PAI-1 (as a vessel marker), as well as the
99 amyloidotropic dye Thioflavin S. Two antibodies against ASC (polyclonal AL-177 and monoclonal
100 MAB/MY6745 anti-ASC) and two antibodies against SAA (MAS41676 and DM003) were employed. We
101 focused on areas in the proximity of vessels of an AA amyloidosis patient (**Fig. 1C**-**E**) and a control
102 patient (**Fig. 1F** and **1G**). The integrated density, defined as the sum of the pixel values in
103 immunofluorescence images, of ASC was slightly increased for the patient with amyloidosis. Both
104 antibodies targeting SAA displayed a signal increase (**Fig. 1H**). The thioflavin S signal colocalized with
105 SAA in the patient with AA amyloidosis, and to a lesser degree with ASC (**Fig. S1A**).

106 We then examined regions of high SAA intensity, presumptively corresponding to amyloid aggregates,
107 by stimulated emission depletion (STED) microscopy (**Fig. 1I**-**L**). The resulting 3D model (**Fig. 1J** and **1L**)
108 visualized the proximity of SAA and ASC within these aggregates. ASC was localized primarily in the
109 periphery of amyloid aggregates, whereas SAA resided mostly in the amyloid cores. This differs from
110 findings reported for ASC-Aβ colocalization, where ASC was found at the core of the plaque [15]. A
111 graphical representation of the geolocation of the center of mass of pixels in space indicated a high
112 distributional overlap between ASC and SAA (**Fig. S1B** and **S1C**). This provides evidence for the

113 colocalization of ASC and SAA in human cardiac tissue affected by inflammation-associated

114 amyloidosis.

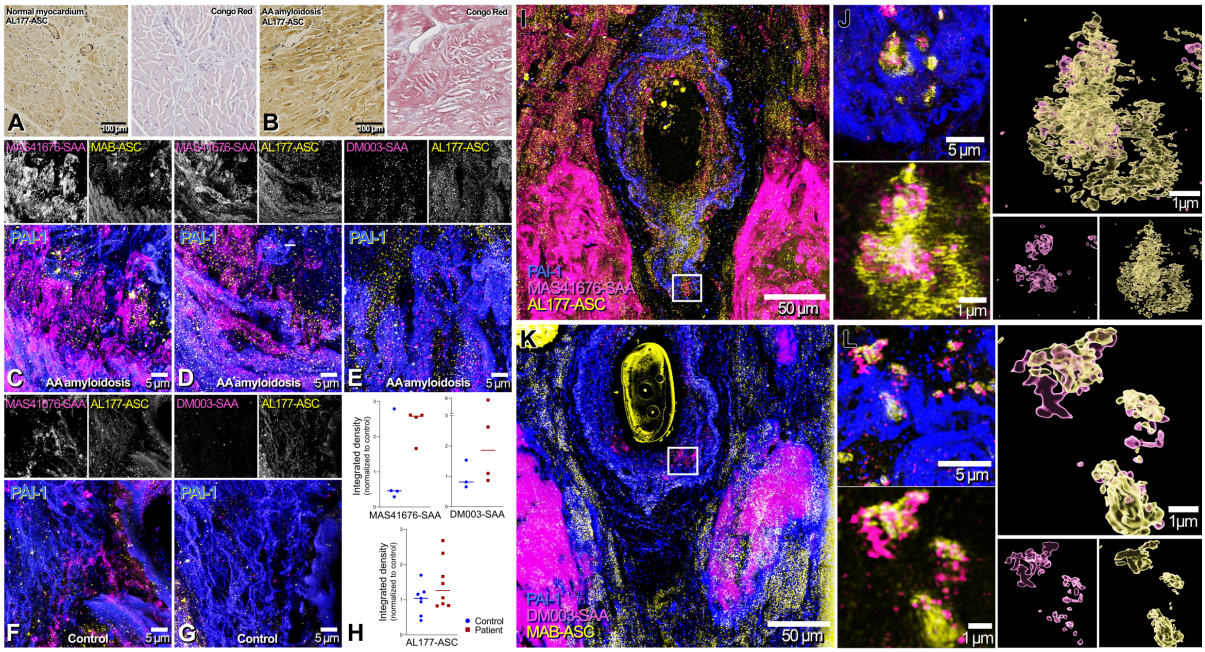

Losa et al., Figure 1

Fig. 1. Co-aggregation of ASC and SAA in human inflammation-associated AA amyloidosis. (A-B) ASC and Congo-red stained myocard from patients without (A) and with AA amyloidosis (B; 68 and 82-year old males, respectively) **(C-E)** Individual and merged confocal images of cardiac blood vessels (labeled with PAI1) from post-mortem tissue of patient with AA amyloidosis, presenting high level of SAA (labeled with MAS41676 and DM003) and ASC (labeled with AL177 and MAB/MY6745). **(F-G)** Individual and merged confocal images of cardiac blood vessels (labeled with PAI1) from post-mortem tissue, presenting low level of SAA (labeled with MAS41676 and DM003) and ASC (labeled with AL177). **(H)** Graphical representation of the quantification of 100X confocal images for SAA and ASC. Each point represents one field of view, bars represent median. Integrated density was normalized by the mean value control. We have refrained from performing a statistical analysis as we provide data from one patient in each group. **(I)** Confocal images from post-mortem tissue of patient with AA amyloidosis showing accumulation of both SAA (MAS41676, magenta) and ASC (AL177, yellow) within the blood vessel border (labeled with PAI1) and in adjacent muscle cells. **(J)** STED imaging of co-aggregation SAA (magenta) and ASC (yellow). Imaris 3D model shows the intricacy of SAA and ASC within these aggregates. **(K)** Confocal images from post-mortem tissue of patient with AA amyloidosis showing accumulation of both SAA (DM003, magenta) and ASC (MAB-ASC (MY6745), yellow) within the blood vessel border (labeled with PAI1) and in adjacent muscle cells. **(L)** STED imaging of co-aggregation of SAA (magenta) and ASC (yellow). Imaris 3D model shows the intricacy of SAA and ASC within these aggregates.

115

116 ***ASC specks interact with SAA through the pyrin domain to promote AA amyloid fibrillation***

117 The colocalization between ASC and SAA raises the question whether ASC may promote AA amyloid

118 formation. We therefore performed *in vitro* SAA aggregation assays. First, murine recombinant SAA

119 protein (mSAA1) and Thioflavin T (ThT) were incubated in the presence of ASC specks or of bovine

120 serum albumin (BSA) (**Fig. 2A**, upper panel). As we observed an accelerated amplification of mSAA1 in

121 the presence of ASC but not of BSA, we performed a dose-response experiment with 0-500k ASC specks

122 (**Fig. 2A**, lower panel). Data were fitted using a four-parametric logistic regression. We observed that

123 a higher number of ASC specks resulted in a left shift of the aggregation curve. In contrast, 500k ASC
124 specks without mSAA did not induce any increase in ThT fluorescence (**Fig. 2A**, upper panel). To
125 quantify the time at which the aggregation of murine SAA reached 50% of its plateau value (termed
126 $t_{1/2}$), we performed global fitting using the AmyloFit software on each of the replicates individually. We
127 found that $t_{1/2}$ was dose-dependently reduced by ASC specks, with higher doses leading to a significant
128 reduction in $t_{1/2}$ (adjusted *p*: 0.013-0.048, Wilcoxon rank sum test with Holms correction for multiple
129 comparisons, **Fig. 2B**). Hence the presence of ASC specks, but not of BSA, accelerates SAA fibril
130 formation. To confirm direct interaction and to map the protein domains of interaction between ASC
131 and SAA, we employed the limited proteolysis-coupled mass spectrometry (LiP-MS) technology [31-36]
132 which detects changes in peptide cleavage exerted by limited proteinase K (PK)-based proteolysis by
133 mass spectroscopy (MS) [37]. If an interaction between proteins exists, certain epitopes become
134 inaccessible to PK and the peptides detected by MS will display an altered profile (**Fig. 2C**). First, we
135 compared the $\log_2$ fold change of peptide representation of PK and trypsin-digested recombinant full-
136 length ASC in the presence or absence of recombinant human SAA1 (**Fig. 2D**), with $|\log_2$ (fold
137 change)$|>1$ and $-\log_{10}$(FDR-adjusted p-value) <0.05 as cutoffs for significance. Five significant changes
138 in the ASC protein were identified (**Fig. 2D**, top, red color), all of which mapped to the pyrin domain of
139 ASC and to part of the linker between pyrin and CARD domain (**Fig. 2D**, bottom), suggesting that this
140 is the site where the protein-protein interaction with SAA occurs. The utilization of recombinant SAA1
141 fibrils instead of the monomeric form closely recapitulated the phenotype (**Fig. 2E**, top), but the linker
142 site seemed to be more involved in the interaction (**Fig. 2E**, bottom). To validate the interaction
143 between ASC and SAA1 also in a complex cellular background, we then incubated lysate of ASC-speck-
144 producing ExpiHEK cells with recombinant human SAA1 and performed the LiP-MS workflow on control
145 lysate and on lysate incubated with SAA1. Among all the interactors of SAA1 (419 LiP-MS hits) in
146 ExpiHEK cells (**Fig. 2F**, blue points) we detected two peptides (red points) from the same region of ASC
147 sequence. Although the altered peptides were slightly different from those of recombinant ASC, the
148 pyrin domain (PYD) was again structurally changed, suggesting that it represents the site of interaction

149 with SAA1 (**Fig. 2F**). The PYD is also the site of interaction with Aβ [15], whereas the CARD domain is

150 known to interact with the CARD of Caspase-1 [38, 39].

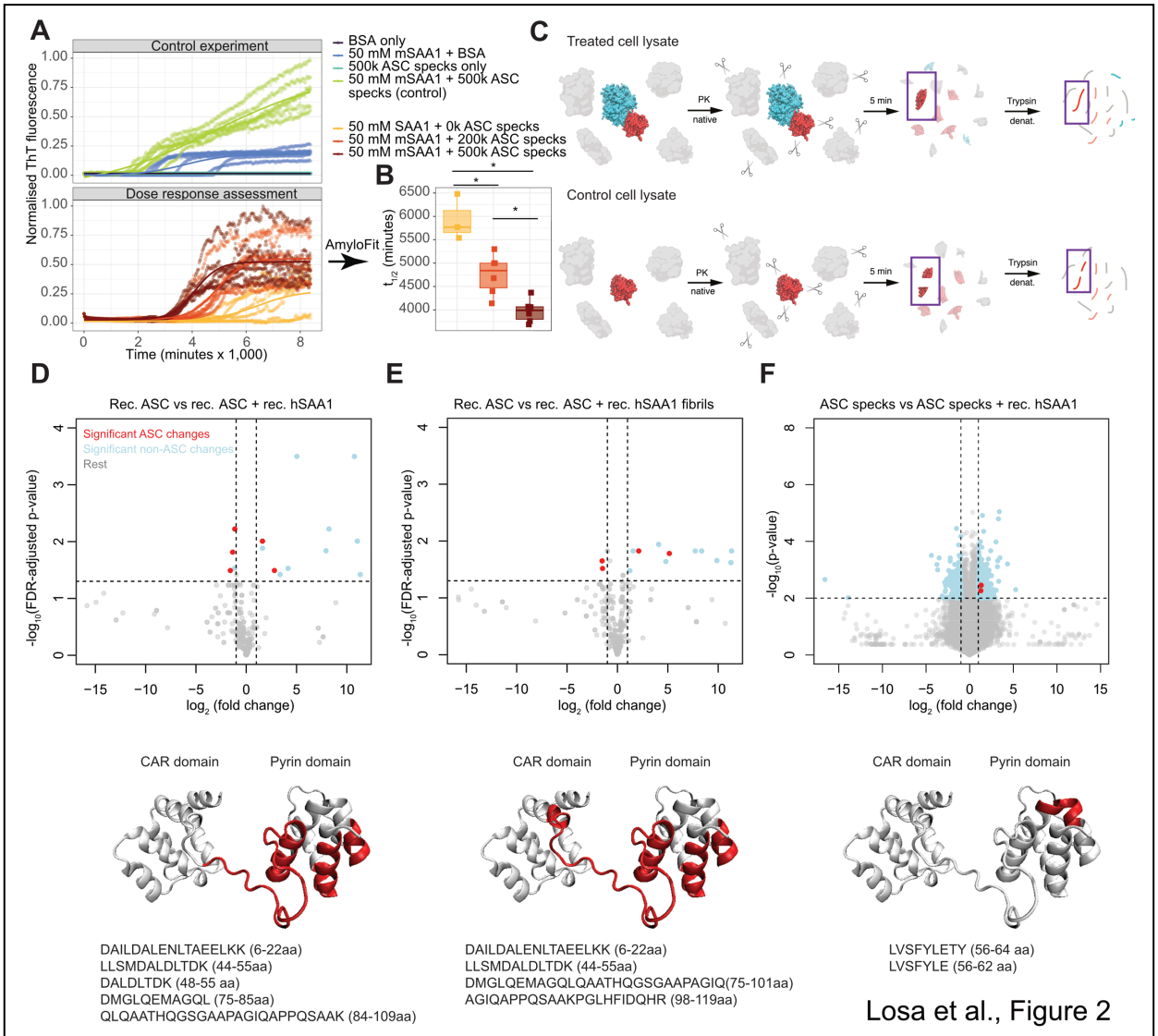

Fig. 2. ASC contacts specific SAA epitopes and accelerates SAA fibrillation. (A) *In vitro* SAA aggregation in the presence or absence of ASC specks over 150 hours. Each curve represents one technical replicate. **(B)** Latency to half-maximal fluorescence signal ($t_{1/2}$) for 0, 200k and 500k ASC specks. Boxplots: median and interquartile ranges (Wilcoxon rank sum test with Holm correction for multiple comparisons). Each dot represents one measurement. *: $p<0.05$. (**C**) Overview of LiP-MS. **(D-F)** Volcano plots (top) and ASC 3D structures (bottom) showing the affected epitopes (red) and respective amino acid sequences after mixing monomeric recombinant human ASC with monomeric recombinant human SAA1 (D), monomeric recombinant human ASC with recombinant human SAA1 fibrils (E), or human ASC specks with monomeric recombinant human SAA1 (F). Ordinate; FDR-adjusted (D-E) and unadjusted p-values (F); unpaired two-tailed t-test. In (D-F), the colours denote the following: Red – significant changes in the ASC protein. Light blue – significant changes other than in the ASC protein. Grey – rest, i.e. non-significant changes.

151

152 ***ASC does not modulate the induction of SAA by $AgNO_3$ or AEF***

153 We injected $AgNO_3$ and amyloid-enhancing factor (AEF), consisting of preformed AA fibrils, into 12

154 male and 10 female wild-type (*Pycard*$^{+/+}$), and into 14 male and 10 female B6.129-*Pycard*$^{tm1Vmd/tm1Vmd}$

155 (*Pycard*$^{-/-}$) littermate mice (**Fig. 3A**). Mice subjected to $AgNO_3$ and AEF injection were denominated
156 "AA$^+$ mice". For control, mice were injected with either PBS, AEF, or $AgNO_3$ only. These mice were
157 collectively denominated "AA$^-$ mice".
158 ASC might increase AA amyloid deposition by favoring its aggregation, or by enhancing SAA induction
159 by inflammatory stimuli. Al^{3+}-containing adjuvants activate the NLRP3 inflammasome, but it is not
160 known whether $AgNO_3$ stimulates ASC-dependent inflammasomes of innate immune cells [40], which
161 would be a confounder in the current study. Thus, we assessed SAA levels of $AgNO_3$-only or AEF-only
162 injected (i.e., AA$^-$) *Pycard*$^{+/+}$ and *Pycard*$^{-/-}$ mice by enzyme-linked immunosorbent assay (ELISA) and
163 compared their SAA serum concentrations at baseline and up to 96 hours after injection. Serum
164 concentrations of SAA and other acute-phase proteins peaked at approx. 24 hours after the
165 proinflammatory stimulus (**Fig. 3B**). There was no significant difference in SAA serum concentration
166 between *Pycard*$^{+/+}$ and *Pycard*$^{-/-}$ mice treated with only $AgNO_3$ or with only AEF at peak and at any of
167 the time points investigated (Wilcoxon rank sum test, **Fig. 3B**). Hence, the genetic ablation of *Pycard*
168 does not affect $AgNO_3$-induced SAA levels, suggesting that ASC-dependent inflammasomes do not
169 significantly contribute to $AgNO_3$ sensing. Moreover, AEF alone was insufficient to induce serum SAA
170 levels in an ASC-dependent manner. We deduce that the anti-amyloidogenic properties of ASC ablation
171 is not due to a modulation of SAA induction.
172
173 ***$AgNO_3$-induced acute-phase responses in Pycard$^{-/-}$ and Pycard$^{+/+}$ mice***
174 Having established the absence of a bias induced by $AgNO_3$ or with only AEF, we assessed SAA serum
175 levels of *Pycard*$^{+/+}$ and *Pycard*$^{-/-}$ mice at baseline and 9, 24, 48, 72- and 96-hours post injection of $AgNO_3$
176 and AEF (i.e., AA$^+$) (**Fig. 3A**). There was a significant difference in SAA levels at 24 hours post injection
177 (hpi) at the peak time of serum acute-phase protein levels [4, 41], between *Pycard*$^{+/+}$ and *Pycard*$^{-/-}$ AA$^+$
178 mice ($p = 0.004$, Wilcoxon rank sum test, **Fig. 3B**. At 0-9 hpi (hours post injection) there was no
179 difference between mean SAA serum concentrations in *Pycard*$^{+/+}$ and *Pycard*$^{-/-}$ mice. However, at 24
180 hpi SAA serum levels of $AgNO_3$-treated *Pycard*$^{+/+}$ mice were significantly higher than in *Pycard*$^{+/+}$ mice

181 treated with $AgNO_3$+AEF (p = 0.03, Wilcoxon rank sum test). This suggests a "sink effect" by which SAA

182 is recruited by AEF and/or by nascent amyloid, and therefore decreases in serum. Crucially, this

183 reduction in SAA serum concentration did not occur in *Pycard*$^{-/-}$ AA^{+} mice. The mean SAA serum

184 concentrations of *Pycard*$^{-/-}$ AA^{+} mice were marginally higher than those of $AgNO_3$-only injected

185 *Pycard*$^{-/-}$ groups at 9, 24, 48 and 72 hpi, possibly because the ELISA detected some inoculated AA fibrils

186 that may still have been present in the bloodstream. At 48 hpi, SAA serum concentrations decreased

187 in all experimental groups. However, at this time point the difference between *Pycard*$^{+/+}$ and

188 *Pycard*$^{-/-}$ AA^{+} mice was still significant (p = 0.009, Wilcoxon rank sum test, **Fig. 3B**). Depending on the

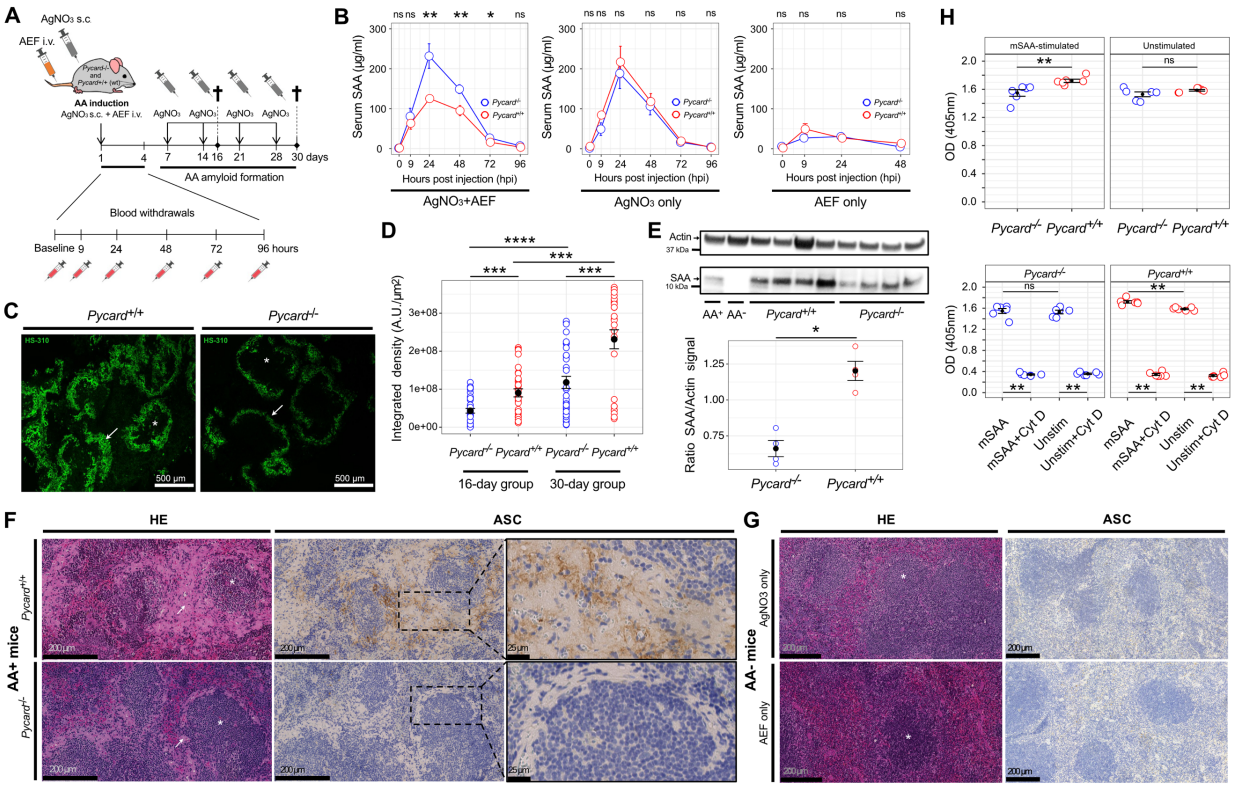

Fig. 3. Decreased splenic amyloid load in the absence of ASC. **(A)** Experimental design. **(B)** SAA serum concentrations (mean ± SEM; triplicates; Wilcoxon rank sum test) in *Pycard*$^{+/+}$ and *Pycard*$^{-/-}$ mice after injection of $AgNO_3$, AEF, or $AgNO_3$+AEF (AA amyloid induction). **(C)** AA^{+} (*Pycard*$^{+/+}$ and *Pycard*$^{-/-}$; P30) spleens stained with LCP (green). Arrows: red pulp invasion of amyloid. Asterisks: follicles. **(D)** Quantification of splenic LCP signal. Dots: individual mice. Scatterplots: mean ± SEM (error bars); Wilcoxon rank sum test with Holms correction for multiple comparisons. **(E)** Top: Western blot of monomeric SAA in spleen homogenates of *Pycard*$^{+/+}$ and *Pycard*$^{-/-}$ mice. Spleen homogenate from non-induced (AA^{-}) and AA^{+} C57BL/6 wt mice served as negative and positive control, respectively. Bottom: Quantification of Western blot data, from four mice per group. mean ± SEM; Kruskal-Wallis test. **(F)** Spleen sections stained with HE and ASC IHC from *Pycard*$^{+/+}$ (wt) and *Pycard*$^{-/-}$ AA^{+} mice. Arrows: amorphous amyloid structures. Asterisks: splenic follicles. ASC with brown stain in IHC. Boxes are magnified in the right panels. **(G)** Spleen sections stained with HE and ASC from *Pycard*$^{+/+}$ AA^{-} mice. **(H)** Phagocytic activity (OD) from unstimulated and mSAA-stimulated *Pycard*$^{+/+}$ and *Pycard*$^{-/-}$ BMDMs specimens. Each assay was carried out in duplicates. Cyt D: 10 µM Cytochalasin D. Mean ± SEM (error bars). Wilcoxon rank sum test with Holms correction for multiple comparisons. Dots: individual bone-marrow samples. * p<0.05, ** p<0.01, *** p<0.001, **** p<0.0001, ns: not significant.

189 genotype, the difference between SAA serum concentrations in *Pycard*$^{+/+}$ and *Pycard*$^{-/-}$ AA^{+} mice
190 persisted up to 72 hours after injections (p = 0.03, **Fig. 3B**). Finally, 96 hours after injection there was
191 no difference in SAA serum concentration. *Pycard*$^{-/-}$ AA^{+} mice were found to have the highest SAA
192 serum concentration among all experimental groups (**Table S2**). We conclude that ASC facilitates the
193 recruitment and deposition of SAA in murine inflammation-associated amyloidosis.
194
195 ***Decreased splenic amyloid deposition in the absence of ASC-dependent inflammasomes***
196 We assessed the presence of amyloid in spleens of mice with experimental AA amyloidosis (**Fig. 3A**) by
197 staining histological sections of paraffin-embedded tissue with Congo red (CR) (**Fig. S2**) and with the
198 luminescent conjugated polythiophene (LCP) HS-310 (**Fig. 3C** and **S3**). We sacrificed experimental
199 animals at day 16 or 30, two days after the last $AgNO_3$ injection. CR-stained amyloid showed the
200 characteristic red appearance in bright-field microscopy and apple-green birefringence under
201 polarized light, similarly to human myocardial tissue (**Fig. 1**). The red spleen pulp of *Pycard*$^{+/+}$ AA^{+} mice
202 exhibited more pronounced amyloid invasion than that of *Pycard*$^{-/-}$ AA^{+} mice (white arrows), and no CR
203 and LCP staining was detected in AA^{-} mice (**Fig. S2** and **S3**). The quantification of HS-310 fluorescence
204 intensity confirmed a significant difference in the amyloid load of *Pycard*$^{+/+}$ and *Pycard*$^{-/-}$ AA^{+} mice at
205 day 16 and 30 (adjusted p = 0.002 and 0.001, respectively; Wilcoxon rank sum test with Holms
206 correction for multiple comparisons) indicating that AA deposition is ASC-dependent (**Fig. 3D**). The
207 median difference increased over time from 2.3-fold (interquartile range (IQR): 0.8-2.7) at day 16 to
208 3.4-fold (IQR: 1.5-6.9) at day 30.
209 Using Western blot (WB), we assessed the presence of the AA amyloid precursor protein SAA in spleen
210 homogenate of the four *Pycard*$^{+/+}$ and *Pycard*$^{-/-}$ AA^{+} mice with the highest splenic amyloid load of the
211 30-days group (**Fig. 3E**). We observed a reduction of total splenic SAA in *Pycard*$^{-/-}$ AA^{+} mice. The median
212 reduction was 1.9-fold (IQR: 1.7-2.1). Like human AA aggregates, we found ASC immunoreactivity
213 adjacent to amyloid deposits (**Fig. 3F**). No amyloid or ASC signals were detected in AA^{-} mice of similar
214 age injected with either PBS, $AgNO_3$ or AEF (**Fig. 3G** and **S4**). ASC immunoreactivity was mostly detected

215 in the perifollicular region of *Pycard*$^{+/+}$ AA^{+} spleens (**Fig. 3F**). These data indicate that the AA amyloid
216 load is strongly modulated by *Pycard*.
217
218 ***No specific transcriptional signature in macrophages upon amyloidosis induction***
219 Prolonged elevation of serum SAA is required to trigger AA amyloidosis [42]. AA aggregates then
220 progressively disrupt tissue integrity and ultimately impair the physiological function of affected
221 organs. Furthermore, patients with systemic AA amyloidosis may exhibit altered red blood cell and
222 platelet volumes [43, 44], which in turn can activate inflammasomes and boost the inflammasome capacity
223 of macrophages, neutrophils and monocytes [45]. We therefore assessed the cellular composition of the
224 spleen and of peripheral blood at baseline and after induction of experimental AA amyloidosis in
225 *Pycard*$^{+/+}$ and *Pycard*$^{-/-}$ mice.
226 Using flow cytometry, we counted splenic B cells, T cells, dendritic cells, neutrophils as well as M1- and
227 M2-like macrophages. Mice that had only been treated with $AgNO_3$ and AA^{+} mice showed increased
228 splenic macrophage infiltration compared to baseline. Macrophage infiltration was neither dominated
229 by M1- nor by M2-like macrophages (**Fig. S4**). We assessed the transcriptional state of fluorescence-
230 activated cell sorted (FACS) splenic macrophages from *Pycard*$^{+/+}$ and *Pycard*$^{-/-}$ AA^{+} mice by RNA
231 sequencing (**Fig. S5A** and **S5B**). Significant ($p < 0.05$; FDR < 0.01) transcriptional changes were only
232 found in the *Pycard* gene, as expected, as well as in *Gdpd3* (**Fig. S5C** and **S5D**), a glycerophosphodiester
233 phosphodiesterase of unknown relevance in the context of SAA. The absence of a distinct macrophage
234 signature in inflammation-associated amyloidosis suggests that other inflammation-related proteins,
235 such as cytokines, may not play an important role in AA formation and deposition.
236
237 ***Reduced phagocytic activity of SAA-activated Pycard$^{-/-}$ bone marrow-derived macrophages***
238 Macrophages and monocytes play a central role in AA amyloidosis. They colocalize with AA amyloid in
239 the spleen of AA^{+} mice [26] and can transfer AA amyloidosis *in vivo* [46]. Conversely, phagocyte depletion
240 delays or inhibits AA amyloid accumulation [25, 29]. Moreover, AA amyloid undergoes Fcγ-receptor-

241 mediated phagocytosis by macrophages, which is initiated by host-specific antibodies that target the
242 AA protein [30]. Since SAA activates macrophages [22-24], and *Pycard*$^{+/-}$ astrocytes of APP/PS1 transgenic
243 mice overexpressing mutant amyloid β precursor protein and presenilin-1 (a mouse model of
244 Alzheimer's disease) show increased Aβ phagocytosis [47], we investigated whether the presence or
245 absence of ASC, in the context of SAA induction, influences the phagocytic activity of murine bone-
246 marrow derived macrophages (BMDMs) *in vitro* (**Fig. S6A** and **S6B**). We exposed SAA-activated and
247 non-SAA-activated murine BMDMs to an *in vitro* phagocytosis assay. There was no significant
248 difference in phagocytic activity between unstimulated *Pycard*$^{+/+}$ and *Pycard*$^{-/-}$ BMDMs ($p = 0.4$,
249 Kruskal-Wallis test) (**Fig. 3H**). However, activity was higher in SAA-stimulated than in unstimulated
250 *Pycard*$^{+/+}$ BMDMs ($p = 0.002$) but not in SAA-stimulated compared with unstimulated *Pycard*$^{-/-}$ BMDMs
251 ($p = 0.589$), suggesting that SAA is partially ASC-dependent in triggering phagocytosis. Furthermore,
252 SAA-stimulated *Pycard*$^{+/+}$ BMDMs showed higher phagocytic activity than *Pycard*$^{-/-}$ BMDMs (p=0.002),
253 underlining a functional implication of the ASC protein (**Table S4**).
254 We considered that the ablation of *Pycard* may cause pathologies of cellular compartments that do
255 not require a direct ASC-SAA interaction. We assessed lymphocyte, monocyte, granulocyte, red blood
256 cell and platelet counts in peripheral blood of AA^{+} and AA^{-} experimental animals (**Fig. S7** and **S8**). Of
257 special interest were myeloid cells as well as platelets. The former form the cellular substrate of
258 *Pycard*-dependent inflammasomes [48] whereas the latter were shown to be key for enhancing
259 inflammasome activation and capacity of innate immune cells upon PRR stimulation [45]. Platelet count
260 at baseline was higher in *Pycard*$^{-/-}$ than in *Pycard*$^{+/+}$ mice ($p = 0.017$). The same was observed for
261 *Pycard*$^{-/-}$ AA+ mice from the 30-days group ($p = 0.036$, **Fig. S8**). The reduction of SAA-induced
262 phagocytosis in *Pycard*$^{-/-}$ BMDMs (compared to *Pycard*$^{+/+}$ BMDMs) supports the notion that ASC is
263 responsible for the modulation of AA amyloid deposition.
264
265 ***Anti-ASC immunotherapy diminishes inflammation-associated amyloid deposition***
266 Therapeutic antibodies can interfere powerfully with amyloid formation [49]. We therefore asked
267 whether treatment with anti-ASC antibodies can reduce AA amyloidogenesis in mice (**Fig. 4A**). We

268 generated a rabbit monoclonal anti-murine ASC antibody targeting the pyrin domain (PYD) and
269 replaced its rabbit Fcγ domain with that of a mouse IgG_{2a} domain to avoid xenogeneic anti-drug
270 responses in recipients and to improve its effector functions *in vivo*. The engineered antibody (denoted
271 MY6745) showed high affinity binding to murine ASC^{PYD} (**Fig. S9A**). Purified, endotoxin-free mouse
272 monoclonal anti-murine ASC and mouse monoclonal isotype control antibody were diluted in PBS to
273 2 mg/ml and intravenously injected (5 mg/kg body weight) at an interval of 7 days. Anti-ASC antibody
274 serum levels were determined at various time points up to 96 hpi after the first injection and were
275 found to peak at 24 hpi (**Fig. 4B**). Western blotting revealed that treatment of *Pycard*$^{+/+}$ AA^{+} mice with
276 antibody MY6745, but not with a non-specific monoclonal isotype-control antibody, reduced total
277 splenic SAA 2.3-fold (IQR: 1.7-3.0, p = 0.01, Kruskal-Wallis test, **Fig. 4C**). Following qualitative amyloid
278 assessment on HE-stained sections (**Fig. 4D**) we performed ASC immunohistochemistry. The anti-ASC
279 antibody treatment significantly diminished the ASC immunohistochemical signal in spleens of
280 *Pycard*$^{+/+}$ AA^{+} mice (**Fig. 4E**), indicating effective target engagement and modulation. The groups
281 significantly differed ($p = 9.9 \times 10^{-5}$, Kruskal-Wallis test, **Fig. 4F**) and the median reduction was 2.7-fold
282 (IQR: 2.4-4.8) compared to the untreated group (with 1.3-fold (IQR: 1.0-1.4) reduction for of the
283 isotype-treated group). Following a quantitative assessment of mature extracellular amyloid, LCP-
284 stained (**Fig. 4G**) spleen sections showed a conspicuous reduction in amyloid deposition of anti-ASC
285 treated AA^{+} mice (p = 0.007, Kruskal-Wallis test, **Fig. 4H**). Importantly, anti-ASC antibody treatment
286 had a strong effect, with a 2.5-fold (IQR: 2.4-3.3) reduction compared to the untreated condition,
287 whereas the isotype-treated group only displayed a 1.2-fold (IQR: 1.1-1.7) reduction in amyloid
288 deposition. Furthermore, AA^{+} mice treated with anti-ASC antibodies experienced a trend towards less
289 severe loss of body weight than non-treated isotype-antibody injected AA^{+} mice, although the
290 differences were not statistically significant (Kruskal-Wallis test, **Fig. S9B**). We conclude that anti-ASC
291 treatment reduces AA amyloid deposition similarly to the ablation of *Pycard*.

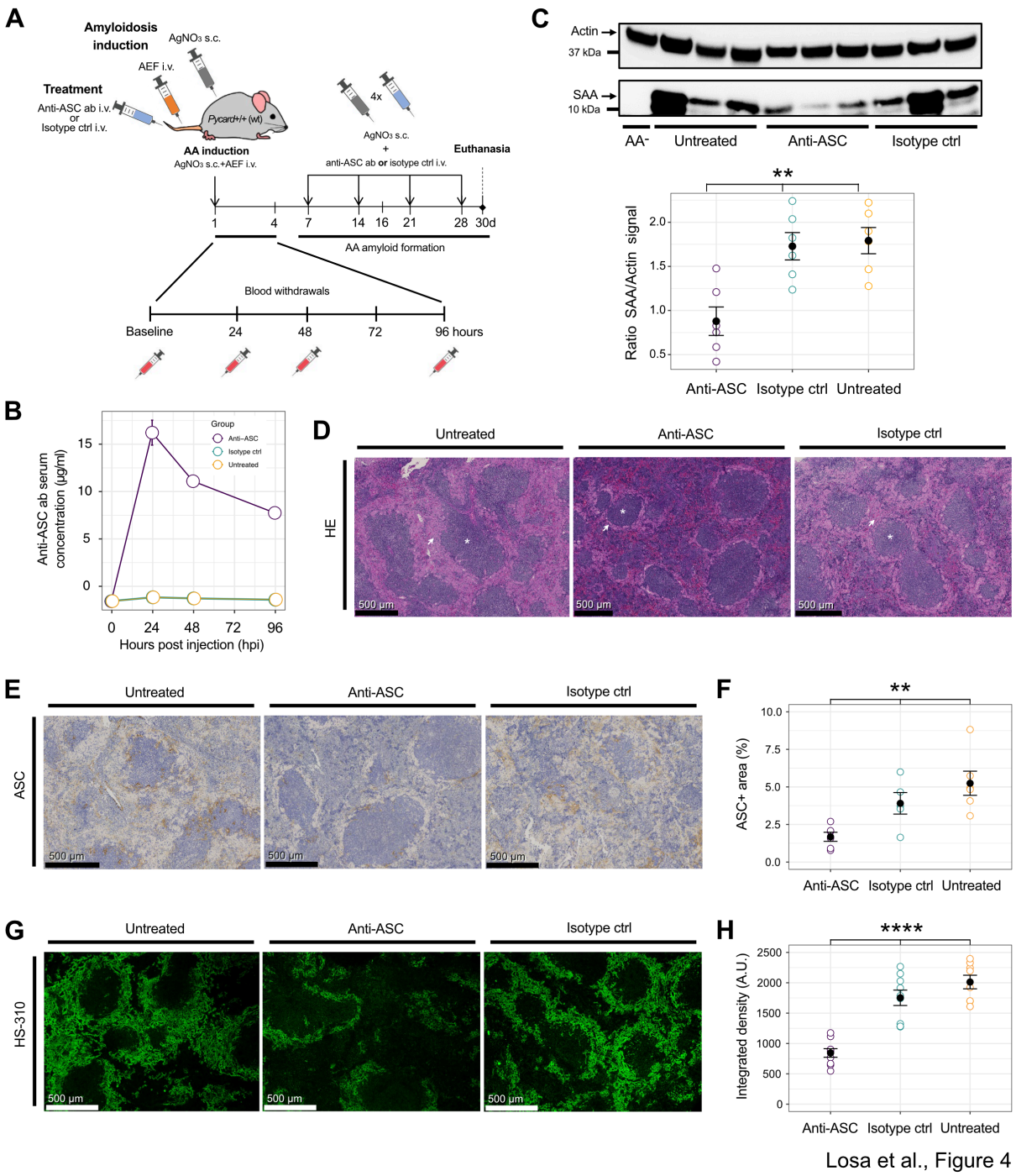

Fig. 4. **Anti-ASC immunotherapy reduces amyloid load**. **(A)** Scheme of anti-ASC immunotherapy. **(B)** Anti-ASC antibody single-injection pharmacokinetics. **(C)** Western blot of SAA in spleen homogenate of *Pycard*$^{+/+}$ AA^{+} mice treated with anti-ASC or isotype antibody, or untreated. Absence of amyloidosis induction as control (AA^{-}). Actin and spleen homogenate from a C57BL/6 wt mouse served as negative control. Scatterplots show data from three mice/group and two independent immunoblots (technical duplicates; mean ± SEM, Kruskal-Wallis test). **(D)** HE-stained spleen sections of *Pycard*$^{+/+}$ AA^{+} mice. Arrows: amyloid. Asterisks: white pulp. **(E)** Spleen sectiond stained with ASC antibodies (brown). **(F)** Quantification of ASC-positive areas in spleen sections. Two fields of view, each representing a different section for each mouse (3 mice/group) were quantified. Scatterplots: mean ± SEM. Statistics: Kruskal-Wallis test. **(G)** Spleen sections stained with LCP. **(H)** Integrated density expressed as arbitrary units/µm^2 in LCP-stained spleen sections. Each dot represents a quantified field of view. Three field of views for each animal were analyzed (nine fields of view from three mice per group). Scatterplots: mean ± SEM; Kruskal-Wallis test. * p<0.05, ** p<0.01, *** p<0.001, **** p<0.0001.

292

293 ***A large-scale investigation of anti-ASC autoantibodies in unselected hospital patients advocates***
294 ***stringent immune tolerance against ASC***

295 Autoantibodies against aggregation-prone proteins can be beneficial against pathological protein
296 aggregate but can also precipitate disease [50-52]. Having established that ASC controls the extent of
297 amyloid deposition in inflammation-associated amyloidosis in mice and that ASC interacts with SAA via
298 its PYD, we investigated whether natural anti-ASC antibodies exist in human antibody repertoires. Such
299 autoantibodies could modulate systemic amyloidosis or conceivably other forms of protein
300 aggregation. First, we established a high-throughput micro-ELISA using an automated robotic platform
301 [53], using an ASC protein containing a C-terminal his-tag [15] at a concentration of 1 µg/ml at a well volume
302 of 3 µl for coating. We then interrogated an unselected cohort consisting of 23,450 plasma samples
303 from 19,334 patients admitted to various clinics at the University Hospital Zurich (**Fig. 5A**) for the
304 presence of autoantibodies against monomeric ASC protein. The median age of the patients was 55
305 (interquartile range: 39-68) years and the female:male ratio was 47.3:52.7 (**Fig. 5B**). The largest
306 fraction of samples originated from the department of cardiology, followed by dermatology,
307 rheumatology, and hematology. We first compared the reactivity titers, i.e., the $-\log_{10}(EC_{50})$ or, in short,
308 $p(EC_{50})$ values, of all patients with that of 119 patients with a history of amyloidosis based on ICD-10
309 code E85 ('Amyloidosis – excluding Alzheimer's disease'), including five individuals with AA
310 amyloidosis, and with 21 patients with ICD-10 codes G30 or F00 ('Alzheimer's disease' and 'Dementia
311 with Alzheimer's Disease'). None of the profiles protruded significantly from the collective (**Fig. 5C**,
312 Kruskal-Wallis test with post-hoc Wilcoxon rank sum test). We then conducted an exploratory logistic
313 regression analysis using a Bayesian LASSO [53, 54] on the entire dataset to identify whether, and which,
314 ICD-10 codes are associated with seropositivity. At high specificity ($p(EC_{50})$ threshold value 2), the
315 highest odds ratios were seen with ICD-10 codes E87 ('Other disorders of fluid, electrolyte and acid-
316 base balance'), K58 ('irritable bowel syndrome'), and S69 ('Other and unspecified injuries of wrist and
317 hand'). However, their odds ratios were 1.00 with 95% credible intervals of 0.78-1.61, indicating no
318 effect. We additionally conducted a sensitivity analysis where we lowered the $p(EC_{50})$ cutoffs to 1.7

319 and 1.5, respectively. While lower cutoffs necessarily decrease the specificity of this analysis, we aimed
320 to explore whether noteworthy differences would manifest more markedly. At p(EC_{50}) threshold value
321 1.7, the highest odds ratios were seen with ICD-10 codes J98 ('Other respiratory disorders'), E83
322 ('Disorders of mineral metabolism'), and R04 ('Haemorrhage from respiratory passages'). However,
323 their odds ratios were 1.00 with 95% credible intervals of 0.86-1.64. Only when lowering the p(EC_{50})
324 threshold even further to values that cannot be considered biologically meaningful, some odds ratios
325 started becoming different from 1.00. The three ICD-10 codes most associated with positivity were
326 U99 ('Special screening examination for SARS-CoV-2'), K65 ('Peritonitis'), and E84 ('Cystic fibrosis), with
327 odds ratios of 1.88, 1.33, and 1.31, respectively (see **Fig. S10**). However, these odds ratios entail large
328 95% credible intervals between 0.85 and 3.84. From this data exploration, we conclude that
329 seropositivity at different cutoffs is not significantly associated with disease conditions.
330 By defining, based on previous studies [50], patients with p(EC_{50}) values ≥ 2 with respective fitting error
331 < 20% as seropositive we identified five candidates who exceeded the threshold in the high-throughput
332 screen (**Fig. 5C**, blue dots). The five seropositive candidates were then tested for specificity and
333 reproducibility with an antigen panel. Only patient #5 confirmed reactivity against the ASC protein (**Fig.
334 5D**). The same patient did not show binding to control proteins such as the human recombinant prion
335 protein (PrP_{23-230} or PrP), full-length tau (Tau441), or the natural Ara h 2 allergen but had received
336 multiple SARS-CoV-2 vaccinations, which explains the positivity to the SARS-CoV-2 Spike protein. We
337 then conducted an additional experiment on patient #5, to detail the epitope and account for
338 potentially unspecific binding to the C-terminal his-tag on the ASC protein. Patient #5 displayed p(EC_{50})
339 values ≥ 2 against the full-length ASC protein as well as against the ASC CAR domain (CARD) but not
340 against the ASC Pyrin Domain (PYD), or against his-tagged LAG3 or TIM3 control proteins (**Fig. 5E**).
341 These results suggest that this patient, admitted to the hospital because of an acute relapsing
342 tonsillitis, had elicited a genuine immune response targeting the CARD of the ASC protein. We conclude
343 that the humoral response against the human monomeric ASC protein can indeed occur but is

exceedingly rare (< 0.01%). This indicates a stringent immune tolerance of the human immune system to ASC.

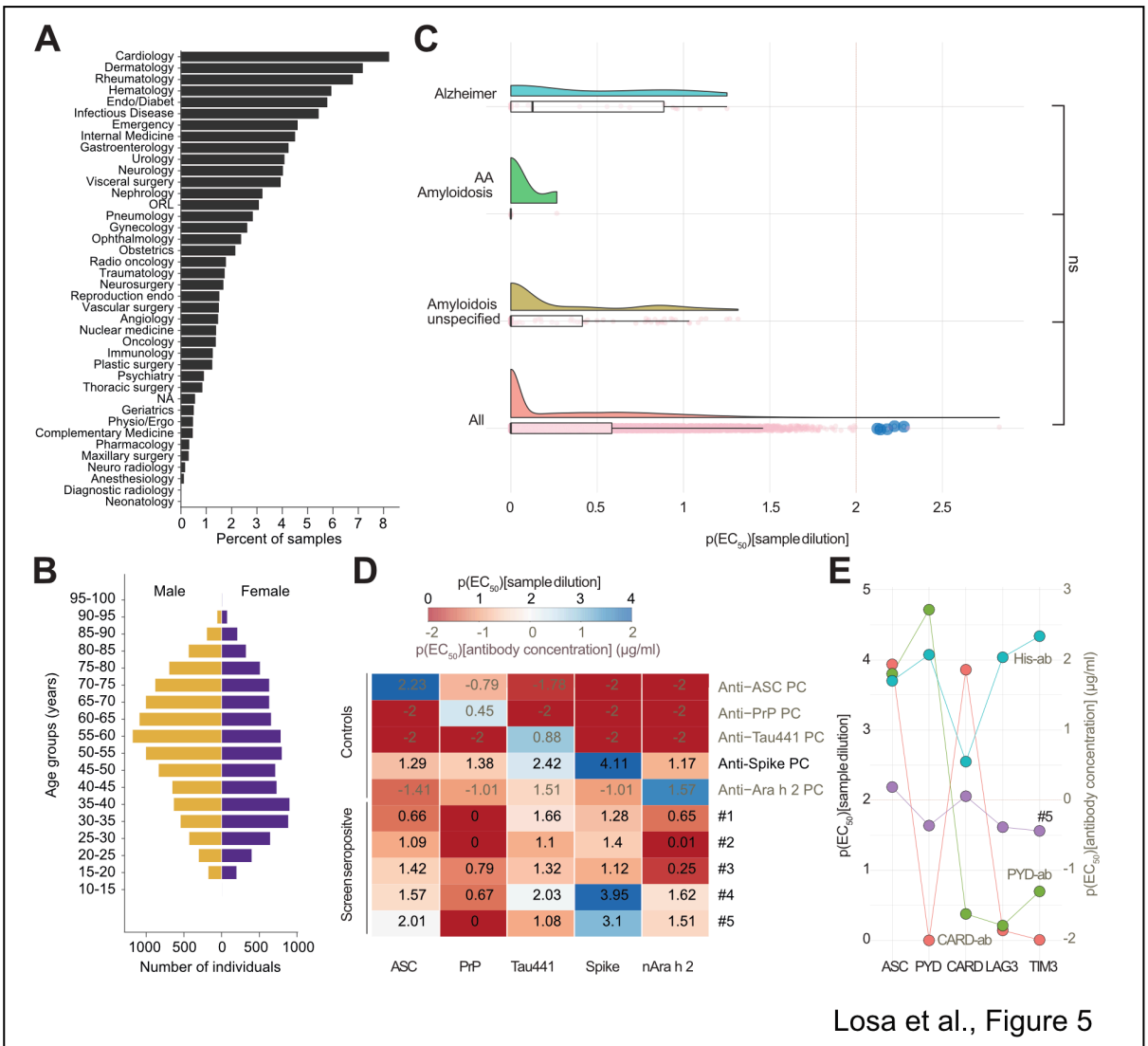

Fig. 5. **Population-wide interrogation of autoantibodies against ASC in a large unselected hospital cohort**. **(A)** Sample provenance by various hospital units. The contributions are depicted as percentage. **(B)** Age distribution of subjects. **(C)** Rainbow/boxplots displaying jittered p(EC_{50}) values for all patients screened (All), for the fraction of patients characterized by ICD-10 code E85 (Amyloidosis), AA amyloidosis, or Alzheimer's disease. Dashed red line at p(EC_{50}) = 2: reactivity cutoff. Blue dots represent the hits, characterized by p(EC_{50}) ≥ 2 and a mean squared residual error < 20% of the actual p(EC_{50}). None of the groups were significantly different (Kruskal-Wallis test *p*-value = 0.079, α = 0.01; Wilcoxon rank sum test *p*-value after Holm correction for multiple comparisons: 0.43 (All vs. Amyloidosis), 0.47 (All vs. AA Amyloidosis), 0.47 (Amyloidosis vs. AA Amyloidosis), 0.47 (All vs. Alzheimer), 0.28 (Amyloidosis vs. Alzheimer), 0.43 (AA Amyloidosis vs. Alzheimer), α = 0.01. **(D)** Heatmap showing p(EC_{50}) values of seropositive samples from screen and controls assayed against an array of antigens. Only the plasma of patient #5 exceeded the cutoff value and was a confirmed binder of human ASC. All samples and controls were assayed as duplicates. (e). Patient #5 (purple), along with multiple control antibodies, was assayed against the full-length ASC protein (ASC), the PY domain of ASC, the CAR domain of ASC, and against LAG3 and TIM3. All proteins used contained a his-tag. All samples and controls were assayed as duplicates. **(D-E)** Two scales are given: (1) For plasma samples, the p(EC_{50}) of the respective plasma dilution is used. (2) For monoclonal antibodies of known concentration, the p(EC_{50}) of the concentrations (in µg/ml) are shown. Anti-ASC, Anti-PrP, and Anti-Tau441 positive control (PC) as well as CARD-ab, PYD-ab, and His-ab are monoclonal antibodies.

347 **Discussion**

348 This study reports the co-aggregation of ASC, the central component of the NLRP3, NLRC4 and AIM2
349 inflammasomes [55, 56], with SAA in tissues of patients with inflammation-associated AA amyloidosis. The
350 role of ASC in AA amyloidosis was investigated in a variety of experimental platforms including super
351 resolution microscopy, AA fibrillization *in vitro*, limited-proteolysis mass spectrometry, and a murine
352 model of inflammation-associated AA amyloidosis. In addition, we explored the potential of
353 immunotherapy against ASC as a pharmacological approach for inflammation-related diseases, such
354 as amyloidosis. Finally, we investigated the prevalence of naturally-ocurring anti-human ASC-
355 autoantibodies on the population level. All the above studies indicate that ASC has a profound effect
356 on the deposition of AA amyloid by interacting with SAA via its pyrin domain.

357 We used STED superresolution microscopy to investigate the topological relationship between ASC
358 and SAA. In contrast with what was observed for amyloid β [15], we found that ASC co-aggregates in the
359 periphery of AA amyloid. But does ASC physically interact with SAA, and if yes, through which epitope?
360 Using an aggregation assay and LiP-MS, we found that the ASC-SAA interaction occurs at a few epitopes
361 located in the pyrin domain of the ASC protein. This finding reflects the literature as the ASC pyrin
362 domain, besides its well-known ASC-homodimerization characteristics [38, 57, 58], is described to be a
363 protein interaction domain [15, 56]. Therefore, it is conceivable that the pyrin domain represents a
364 potential target for therapy development. Since *in vivo* in *Pycard*$^{+/+}$ AA^{+} mice, the deposition of AA
365 amyloid appeared to be more invasive into the red pulp than in *Pycard*$^{-/-}$ AA^{+} mice, we concluded that
366 ASC inflammasome protein assemblies, driven by ASC^{PYD} oligomerization and ASC^{CARD} cross-linking,
367 modulate amyloidogenesis or the deposition of AA amyloids in tissue, similarly to what has been shown
368 for amyloid β [15] and tau [14] elsewhere. It is thus conceivable that ASC serves as a generic protein
369 aggregation enhancing platform in various central and peripheral PMDs where the innate immune
370 system is involved.

371 We probed alternative routes by which ASC could decrease the amyloid load. It is widely recognized
372 that macrophages colocalize with amyloid deposits and that Fcγ-receptor-mediated phagocytosis plays

373 an important role in deposition, processing and clearing of AA amyloid [25, 26, 30, 59, 60]. We found that
374 *Pycard*$^{+/+}$ murine BMDMs showed stronger phagocytosis than *Pycard*$^{-/-}$ BMDMs, similarly to
375 phagocytosis of Aβ in a murine model of AD [47]. In addition, transcriptomic analysis of splenic
376 macrophages of AA diseased mice revealed no significant differentially expressed genes between
377 *Pycard*$^{+/+}$ and *Pycard*$^{-/-}$, and ASC transcripts were only identified in *Pycard*$^{+/+}$ mice, as expected, and
378 there was an increased splenic macrophage infiltration in $AgNO_3$-only (AA^- mice) as well as AA^+ mice at
379 the time of euthanasia, compared to baseline levels, which underscores the involvement of innate
380 immune cells, especially myeloid cells, in the pathogenesis of AA amyloidosis. These findings suggest
381 that the reduced splenic AA amyloid load in *Pycard*$^{-/-}$ mice is mainly due to the absence of ASC rather
382 than enhanced phagocytosis of *Pycard*$^{-/-}$ BMDMs, even if there may be post-translational signatures or
383 transcriptional changes that went unnoticed owing to limited sensitivity.
384 Another contributor to AA formation in chronic inflammation may be HDL-SAA complexes forming
385 when entering the circulation. An *in vitro* ThT-fluorescence aggregation assay showed that HDL
386 protects SAA from aggregation [61]. HDL may sequester SAA in an α-helical dominant conformational
387 state, thereby preventing fibrillogenesis. Moreover, HDL-SAA complexes and monomeric SAA have
388 been shown to be endocytosed into the lysosomal compartment of macrophages, where complex
389 dissociation and self-assembly of SAA into AA protofibrils is initiated [61, 62]. ASC may therefore not only
390 interact with SAA but also with HDL from the HDL-SAA complexes. This interaction may lead to SAA
391 release from these complexes, shifting the equilibrium towards AA formation. Moreover, post-
392 translational modifications such as phosphorylation and ubiquitination of ASC (CARD and PYD) regulate
393 ASC assembly and inflammasome activity in a complex manner [63]. The sum of evidence, therefore,
394 suggests that ASC-dependent acceleration of amyloidogenesis is due to physical amyloid scaffolding
395 and/or to enhanced macrophage-dependent spread of seeds [24].
396 Having discovered that the ASC pyrin domain physically interacts with SAA, we hypothesized that a
397 pharmacological targeting of this domain may recapitulate the results seen in the *Pycard* knockout
398 model, i.e., reduced amyloid deposition. Indeed, anti-ASC^{PYD} antibodies were effective in reducing

399 amyloid load and may represent a viable therapeutic strategy. In this context, anti-ASC^{PYD} therapy
400 might impact the immune function indirectly path and might reduce the visceral AA amyloid load,
401 similarly to a combined therapy with small drugs targeting circulating serum amyloid P component
402 (SAP) and with a monoclonal anti-SAP antibody [60, 64].
403 Finally, in a population-wide anti-ASC autoantibody screen, performed in a cohort of cross-
404 departmental hospital patients, we investigated the humoral B cell response against the human
405 monomeric ASC protein. Any such anti-ASC autoantibodies could for instance neutralize ASC specks
406 that may also form neoepitopes. Consequently, the blockade of ASC could impair AA amyloid
407 formation. We observed that humoral response against ASC is exceedingly rare (< 0.01%), indicating a
408 high tolerance of the human immune system to ASC. Thus, natural anti-ASC autoantibodies are likely
409 not a key player in the modulation of inflammation-associated diseases such as amyloidosis.
410 Conversely, the absence of a natural immune response to ASC may increase the chance of high
411 tolerance as well as successful immunotherapy approaches employing anti-ASC antibodies in
412 inflammatory diseases. Moreover, higher -logEC_{50} values were not associated with any specific ICD-
413 coded diagnosis.
414 In conclusion, this study reports a crucial role for ASC in SAA interaction and recruitment, SAA serum
415 level modulation, SAA fibril formation acceleration, and controlling the extent of inflammation-
416 associated amyloidosis with respect to AA amyloid deposition. It is conceivable that the effect is not
417 only a result of the binding properties of ASC and ASC specks for β-sheet-rich proteins. Alternatively,
418 ASC assemblies may serve as aggregation-enhancing scaffolds in various PMDs. Finally, our findings
419 might have therapeutic implications that advance the fields PMDs and chronic inflammatory diseases
420 in general as ASC could be a target of disease-modifying therapies that aim to reduce amyloid
421 deposition and pathology in various proteinopathies.

422 **Material and Methods**

423 *Histology and immunohistochemistry of human tissue*

424 Formalin-fixed and paraffin-embedded cardiac sections (2-4 µm) were de-paraffinized with three
425 cycles of xylene treatment followed by re-hydration with 100 % EtOH, 96 % EtOH, 70 % EtOH and water
426 (each cycle 5 min) respectively. Hematoxylin and eosin (HE) as well as Congo red (CR) staining and ASC
427 immunohistochemistry (IHC) were performed according to standard procedures used at our institute.
428 IHC was performed with anti-ASC pAb (clone AL177, AdipoGen) at a dilution of 1:500.

429 For confocal and stimulated emission depletion (STED) microscopy, formalin-fixed and paraffin-
430 embedded cardiac sections (15 µm) were de-paraffinized with xylene followed by re-hydration with
431 100 % EtOH, 95 % EtOH, 80% EtOH, 70 % EtOH and 50%EtOH. Sections were block with a 10% donkey
432 serum, 5% BSA PBS 0.02% triton. PAI1 (PA1-9077, ThermoFisher), SAA (MAS-41676, Invitrogen), ASC
433 (clone AL177, AdipoGen) and ASC (MY6745, Mabylon) were used at 1:200 dilution, SAA (DM003,
434 OriGene Technologies) was used at 1:20 dilution, all in saturating buffer, for 48 h at 4 °C. Alexa 488,
435 568 and 647 from Invitrogen were used at 1:200 concentration in saturating buffer, for 24 h at 4 °C.
436 Thioflavin S staining (1%) was performed for 15 min at room temperature. Sections were treated with
437 Sudan Black before mounting in ProLong Diamond Antifade Mountant (ThermoFisher).

438 Confocal and super-resolution STED images were acquired on a Leica SP8 3D, 3-color gated STED laser
439 scanning confocal microscope. 10x (NA 0.3, **Fig. S1**), 20x (immersion Oil, NA 0.75) and 100x (immersion
440 oil, NA 1.4) images were acquired at a resolution of 2048x2048. 10x images were acquired with a 600Hz
441 bidirectional scan yielding a XY resolution of 567.9um per pixel, 20x images were acquired with a 700Hz
442 bidirectional scan yielding a XY resolution of 126.2 µm per pixel, and 100x images with a 1000Hz
443 bidirectional scan yielding a XY resolution of 25.2 µm per pixel. Images were then deconvoluted using
444 Huygens Professional software, and analyzed with image J Fiji. All presented images are max Z-
445 projection and were adjusted for grey values identically for control and AA amyloidosis patient. STED
446 images were visualized using Imaris 10.0.0 version.

447 *Mice*

448 Animal care and experimental protocols were in accordance with the Swiss Animal Protection Law and
449 approved by the Veterinary office of the Canton of Zurich (permits ZH131-16 and ZH188/2020). Mice
450 were bred in a high hygienic grade facility of the University Hospital of Zurich (BZL) and housed in
451 groups of 2-5. Mice were under a 12-hour light/ 12-hour dark cycle (from 7 a.m. to 7 p.m.) at 21 ± 1°C.
452 *Pycard*-deficient mice (B6.129-*Pycard*^{tm1Vmd}) were generated as previously published in Mariathasan,
453 Newton, Monack, Vucic, French, Lee, Roose-Girma, Erickson and Dixit [55]. C57BL/6 wildtype mice were
454 obtained from the Jackson laboratory. To minimize environmental bias and potential differences in
455 microbiota, littermates were bred. We perfomed the experiments with highest possible gender and
456 age congruence among experimental groups (**Table S5-S8**). Mice were randomly assigned to the
457 experiments. In the anti-ASC antibody treatment experiment two mice in each of the antibody injected
458 groups were found dead within the experiment.

459 *Genotype screening*

460 Ear biopsies were digested and subjected to PCR. An 859 bp *Pycard* allele fragment was amplified using
461 forward 5'-GAAGCTGCTGACAGTGCAAC-3' and reverse 5'-CTCCAGGTCCATCACCAAGT-3' primers.
462 Amplification of a 275 bp gDNA fragment from the B6.129-*Pycard*^{tm1Vmd} Neo cassette was done using
463 forward 5'-TGGGACCAACAGACAATCGG-3' and reverse 5'-TGGATACTTTCTCGGCAGGAGC-3' primers.
464 PCR products were run on a 1.5% agarose gel and developed for genotype definition.

465 *AA induction and anti-ASC/isotype antibody injections*

466 Silver nitrate (Merck) was eluted in nuclease-free water (Ambion®). AEF was prepared as previously
467 described [65] and pH was adjusted to 7.4 before administration. AA amyloidosis induction was
468 performed by injections of 100 µl AEF (i.v.) and 200 µl sterile filtered 1 % silver nitrate solution (s.c.)
469 (Merck). Repeated injections of silver nitrate were in accordance with the reference [59]. To asses
470 amyloid load and ASC distribution in *Pycard*$^{+/+}$ and *Pycard*$^{-/-}$ mice AA was induced in 22 *Pycard*$^{+/+}$ and
471 24 *Pycard*$^{-/-}$ mice, and 33 mice were injected with either PBS, $AgNO_3$ or AEF and served as controls (**Fig.
472 3A**). To perform the anti-ASC antibody treatment, a total of 15 Pycard$^{+/+}$ mice were induced with AA

473 ($AgNO_3$ and AEF injections, i.e., AA^+) and additionally injected with either anti-murine ASC antibody or
474 isotype control antibody (**Fig. 4A**). Anti-murine ASC and isotype control antibody were diluted in PBS
475 with at a stock concentration of 2 mg/ml and intravenously injected at a concentation of 5 mg/kg
476 bodyweight. Characteristics of experimental groups in **Table S5**-**S8**. Two mice of the antibody injected
477 groups were found dead within the experiment and were therefore excluded from further analyses.

478 *Mouse serum amyloid A (SAA) measurements*

479 To determine the SAA levels in mice serum, blood was withdrawn into BD Microtainer® SST™ Tubes at
480 baseline and up to 96 hours post injection. Samples were left at room temperature (RT) for 30 min and
481 subjected to centrifugation at 10'000xg for 8 min at 4°C. Serum samples were then transferred and
482 stored at -80°C. SAA levels were assessed by a mouse SAA enzyme-linked immunosorbent assay (ELISA)
483 kit (abcam) according to the manufacturers' guidelines. Mouse serum samples were analyzed in
484 technical triplicates. ELISA plate was developed and the optical density at 450 nm was measured.

485 *Euthanasia and organ harvesting*

486 Upon euthanasia, organs were harvested and kept on ice in Iscove's Modified Dulbecco's Medium
487 (IMDM) (ThermoFisher Scientific) until measurement and further usage (no longer than 4 hours). Bone
488 marrow cells of tibia, femur and pelvis were flushed into IMDM using 25G needles (B. Braun). Tissue
489 was fixated in formalin for paraffin embedding or put in Tissue-Tek® O.C.T.™ compound (Sakura®) for
490 frozen sections.

491 *Histology and immunohistochemistry of murine tissue*

492 Formalin-fixed and paraffin-embedded spleen or cardiac sections (2-4 µm) were de-paraffinized with
493 three cycles of xylene treatment followed by re-hydration with 100 % EtOH, 96 % EtOH, 70 % EtOH and
494 water (each cycle 5 min) respectively. Hematoxylin and eosin (HE) as well as Congo red (CR) staining
495 and ASC immunohistochemistry (IHC) were performed according to standard procedures used at our
496 institute. IHC was performed with anti-ASC pAb (clone AL177, AdipoGen) at a dilution of 1:500. To
497 analyze the ASC-positive area (% of total area) the open-source software QuPath
498 (https://qupath.github.io) was used. To perform LCP staining, slides were incubated with HS-310 for

499 30 min at RT in the dark at a final concentration of 0.3 µg/ml in PBS [66, 67]. After washing, slides were
500 mounted with fluorescence mounting medium (Dako) and subjected to imaging on a fluorescence
501 microscope (OLYMPUS BX61 fluorescence microscope system with an OLYMPUS XM10 camera). The
502 hexameric LCP HS-310 was produced as previously described [68].

503 *Fluorescence and polarized microscopy*

504 To analyze LCP-stained tissue sections, we assessed three different and independent visual fields at 4x
505 magnification and slides per mouse and organ. Two parameters, HS-310 positive area (% of area) as
506 well as the fluorescence integrated density (A.U./μm^2) of HS-310 were calculated with the open-source
507 software ImageJ (https://github.com/imagej/ImageJ). To confirm the presence of amyloid, we
508 assessed the apple-green birefringence of amyloid under polarizing light in Congo red stained spleen
509 tissue sections (**Fig. S2**). FACS sorted splenic macrophages were visually confirmed by filter settings
510 that allowed the detection of PE-Cy5 and APC-Cy7.

511 *SAA immunoblot analysis*

512 To determine SAA presence by WB, spleen tissues from AA induced mice were homogenized in 1:9
513 volumes (w/v) RIPA buffer (50 mM Tris pH 7.4, 1 % NP-40, 0.25 % Deoxycholic acid sodium salt, 150
514 nM NaCl, 1 mM EGTA, protease inhibitors (complete Mini, Roche)) using TissueLyser LT for 45 seconds
515 for four cycles. Samples were cooled on ice between cycles. Supernatant was transferred into new
516 tubes after full speed centrifugation 16000g for 10 min at 4°C. Input (same volume per sample and
517 blot) was boiled at 95°C for 10 min with a final concentration of 1 µM DTT and 4x NuPage™ LDS sample
518 buffer (ThermoFisher Scientific). Spleen homogenate was separated using SDS-PAGE (Novex NuPAGE
519 4-12 % Bis-Tris Gels, Invitrogen) and transferred to a PVDF membrane (ThermoFisher Scientific) at 20
520 V for 7 min. Membrane was blocked with 5 % milk in TBS-T (Tris-Buffered Saline, 0.1 % TWEEN®20, pH
521 7.6) for 3 hours at RT. Primary rabbit anti-SAA antibody was incubated overnight (o/n) at 4°C at a
522 concentration of 2.5 µg/ml (**Table S9**). Actin served as loading control. Membrane was incubated with
523 primary mouse anti-actin antibody (Merck) at a 1:8000 dilution in blocking buffer at 4°C o/n. After 4
524 cycles of washing, membranes were incubated for 1 hour at RT with secondary horseradish peroxidase

525 (HRP)-conjugated goat anti-rabbit IgG (H+L) (Jackson Immuno) and with secondary HRP-conjugated
526 goat anti-mouse IgG (H+L) (Jackson Immuno) diluted 1:5000 and 1:8000 in blocking buffer,
527 respectively. Blots were developed using Luminata Crescendo Western HRP substrate (Milipore) and
528 visualized with the Stella system (model 3200, Raytest) (**Fig. S11** and **S12**).

529 *Production of monomeric ASC in E. coli*

530 Monomeric human ASC-His, ASC-GFP-His and the ASC PYD domain (ASCPYD-His-SII) as well as the ASC
531 CARD domain (ASCCARD-His-SII) were expressed in E. coli and purified from inclusion bodies via Nickel
532 beads. Therefore, E. coli strain BL21(DE3) was transformed with pET-based vectors encoding the his-
533 tagged ASC variants. Expression was done in self-inducing media (MagicMediaTM, Invitrogen)
534 incubated at 37 °C for 1 h and 67 h at 20 °C. Subsequently, cells were harvested by centrifugation at
535 4000rpm for 30min. For cell lysis, the pellet was resuspended in 50 mM phosphate, 300 mM NaCl, pH
536 7.5 and sonicated on ice 10 min at 40% power (2 secpulse/pause). The suspension was then centrifuged
537 at 14000g at 4°C for 30 min to collect the pellet containing the inclusion bodies. To solubilize the
538 inclusion bodies, pellets were resuspended in 50 mM phosphate, 300 mM NaCl, 6 M Gua-HCl, 2 mM
539 DTT, pH 7.5 for 30min at RT. Afterwards the suspension was centrifuged at 14000g at 4 °C for 30 min
540 to remove residual insoluble cell debris. The supernatant was then incubated with Nickel beads
541 (Themo, #88221) for 3 h at RT., The beads were washed once with 50 mM phosphate, 300 mM NaCl,
542 6 M Gua-HCl, 2 mM DTT, pH 7.5 and followed by 50 mM phosphate, 300 mM NaCl, 6 M Gua-HCl, 2 mM
543 DTT, 20 mM imidazole pH 7.5. To elute the His-tagged proteins, beads were incubated with 50 mM
544 phosphate, 300 mM NaCl, 6 M Gua-HCl, 2 mM DTT, 500 mM imidazole pH 7.5. The pH of the eluate
545 was adjusted to pH 3.8 with diluted HCl. Next, the eluate was dialysed against 50 mM Glycine, 150 mM
546 NaCl, pH 3.8 in 3500 Da cassette O/N at 4°C. To remove higher order aggregates, the dialysed samples
547 were purified using a preparative SEC column (HiLoad 16/600 Superdex 75 pg). The monomeric
548 proteins were finally concentrated using a VivaSpin 3000 Da column.

549 *Production and purification of ASC specks*

550 Untagged ASC specks were recombinantly produced similarly to what was previously described [69]. In
551 brief, suspension HEK293 cells were transiently transfected with expression plasmids encoding full
552 length human ASC or ASC-GFP using linear PEI 40 kDa. After 7 days of expression at 37 °C and 5% CO_2,
553 cells were harvested and resuspended in Buffer A (320 mM sucrose, 20 mM HEPES-KOH (pH 7.5), 10
554 mM KCl, 1.5 mM MgCl2, 1 mM, EDTA, 1 mM EGTA. Cells were lysed by syringing (10x 20G, 20x 25G),
555 freeze-thawing (3x), followed by subsequent syringing (20x 25G). Afterwards the lysate was
556 centrifuged at 400g for 8 min, the pellet was resuspended in 2x CHAPS buffer (40 mM HEPES-KOH (pH
557 7.5), 10 mM MgCl2, 1 mM EGTA, 0.2 mM PMSF, 0.2 % CHAPS) and filtered using 5 µm centrifugal filters
558 at 2000g for 10 min. The filtrate was then diluted and gently mixed with 1 volume of 2x CHAPS buffer
559 and centrifuged at 2300g for 8 min. The resulting pellet was resuspended in 1 ml of 1x CHAPS buffer
560 and centrifuged at 5000g for 8 min. This washing step was repeated twice. Afterwards the pellet was
561 resuspended in 1x CHAPS buffer and loaded carefully on the top of 40% Percoll and centrifuged at
562 16000g for 10min. The interface layer containing the ASC speck particles was collected carefully and
563 washed once by centrifugation at 5000g for 3 min and resuspension in 1X CHAPS buffer. Lastly, tag-
564 free ASC specks were stained using an anti-ASC antibody and a fluorescently labelled secondary
565 antibody. Antibody-stained fluorescent particles were quantified in a fluorescence microscope using
566 a Bürker chamber, delivering absolute counts of ASC speck numbers.

567 *ASC speck immunoblot analysis*

568 To assess the purity and the presence of untagged ASC specks used in aggregation assays, purified
569 protein or HEK cell lysate were boiled at 95°C for 10 min with a final concentration of 10 mM DTT
570 diluted in NuPage™ LDS sample buffer (ThermoFisher Scientific). Proteins were separated using SDS-
571 PAGE (Novex NuPAGE 4-12 % Bis-Tris Gels, Invitrogen) and transferred to a PVDF membrane
572 (ThermoFisher Scientific) at 20 V for 7 min. Membrane was blocked with 5 % milk in TBS-T (Tris-
573 Buffered Saline, 0.1 % TWEEN®20, pH 7.6) for 3 hours at RT. Primary rabbit anti-ASC antibody (clone
574 AL177, AdipoGen) was incubated overnight (o/n) at 4°C at a dilution of 1:1000. After 4 cycles of

575 washing, membranes were incubated with secondary horseradish peroxidase (HRP)-conjugated goat
576 anti-rabbit IgG (H+L) (Jackson Immuno) diluted 1:5000 in blocking buffer for 1 hour at RT. Blot was
577 developed as described above (**Fig. S13**).

578 *In vitro SAA fibril formation*

579 Recombinant murine SAA1 was generated as previously described in [61]. The *in vitro* aggregation assay
580 was carried out in a black 96-well plate (Greiner Bio-One, PS, F-bottom, black) on a FLUOstar OMEGA
581 plate reader (BMG Labtech). SAA1 was dissolved in water to achieve a stock solution concentration of
582 10 mg/ml. The final reaction volume was 100 µl per well and consisted of 50 µM murine SAA1, 20 µM
583 Thioflavin T (abcam) and 50 mM Tris buffer pH 8.0. ASC specks (quantified as described above) were
584 diluted in PBS and added at various concentrations. Bovine serum albumin (BSA, Sigma-Aldrich) was
585 dissolved in water to reach a final reaction concentration of 50 µM. The plate was agitated every 20
586 min by orbital shaking for 10 s at 100 rpm. The assay was performed at 37°C. Fluorescence (Ex: 450nm,
587 Em: 490 nm) was measured over the course of 140 hours. We conducted two independent
588 experiments (**Fig. 2A**). ThT fluorescence intensity values were displayed in the following manner: (1)
589 We first transformed the data so that all conditions and repeats started with ThT fluorescence intensity
590 0 at timepoint 0 minutes. (2) We applied a range function separately onto both the control experiment
591 as well as on the dose-response datasets, i.e.

592 $$\frac{x - \min(x)}{\max(x) - \min(x)}$$

593 where x was the adjusted ThT fluorescence intensity and min and max the respective minimum and
594 maximum ThT fluorescence signals in each of the two experiments. This allowed us to obtain data
595 scaled between 0 and 1 for the two datasets individually. The ordinate in **Fig. 2A** is therefore labelled
596 as 'Normalised ThT fluorescence'. (3) To visualize trends over all replicates, we conducted four-
597 parametric logistic regression analyses. (4) For quantification of $t_{1/2}$ values, data were fitted with a
598 global fitting procedure using the software application AmyloFit according to the developer's
599 instructions [70].

600 *Limited proteolysis-coupled mass spectrometry (LiP-MS)*

601 LiP-MS was conducted as shown earlier [31-35]. Briefly, we incubated purified recombinants ASC protein
602 or ExpiHEK cell native lysates containing ASC specks with human recombinant SAA1 proteins for 15
603 min at 37 °C in LiP buffer (100 mM HEPES pH 7.4, 150 mM KCl, 1mM $MgCl_2$). Next, PK was added to
604 each independent technical replicate simultaneously at 1:100 (w/w) enzyme to substrate ratio for 5
605 min at 37 °C. Four technical replicates per condition were done for purified proteins and three for
606 ExpiHEK lysate. To stop limited proteolysis reaction, PK was heat-inactivated by sample incubation at
607 99 °C. Subsequently, samples were transferred into equal volume of 10% sodium deoxycholate (Sigma
608 Aldrich). Next, samples were reduced with 5 mM tris (2-carboxyethyl)phosphine hydrochloride for 40
609 min at 37 °C under 800 rpm shaking, alkylated in 40 mM iodoacetamide, and incubated in the dark at
610 RT for 30 min. Finally, samples were diluted in ammonium bicarbonate and digested with lysyl
611 endopeptidase and trypsin (at enzyme to substrate ration of 1:100) at 37 °C for 17 h under 800 rpm
612 shaking. Digestion was stopped by addition of formic acid (4% final concentration). Precipitate of
613 sodium deoxycholate was removed via centrifugation, samples were desalted with Sep-Pak tC18
614 cartridges (Waters) and eluted with 80% acetonitrile, 0.1% formic acid. Samples were analyzed on an
615 Orbitrap Fusion Lumos Tribrid mass spectrometer (Thermo Fisher) equipped with a nanoelectrospray
616 ion source and an UPLC system (Waters) in data-independent acquisition mode. Spectronaut
617 (Biognosys AG) software was used to search the raw MS data. The statistical data analysis was done in
618 R. Two-tailed t test was applied to assess statistical significance between peptide abundances.
619 Significance cutoffs of $|\log_2$ (fold change)$|>1$ and $-\log_{10}$ (FDR-adjusted p-value) <0.05 or $|\log_2$ (fold
620 change)$|>1$ and $-\log_{10}$ (p-value) <0.05 were used, as indicated. LiP-MS hits corresponding to ASC
621 protein were highlighted in red (**Fig. 2D-F**). Significant peptides originated from other proteins are
622 depicted in blue. The blue data points in **Fig. 2D** and **2E** correspond to contaminants (i) originating from
623 co-purified proteins. (ii) corresponds to SAA protein that was present only in one condition. We
624 focused on significant changes in ASC protein (depicted in red).

625

626 *Differentiation of bone marrow cells to bone marrow derived macrophages (BMDMs)*

627 BMDMs were generated, with slight modifications, as previously published [71]. BM cells were harvested
628 from tibia and femur, washed twice in PBS, and resuspended in differentiation medium I-10 + M-CSF
629 (i.e., IMDM, 10 % FBS, 1 mg/ml Pen/Strep containing 25 ng/ml recombinant murine M-CSF
630 (PeproTech)) at a density of 1-2 Mio. cells/ml. After incubation for four days at 37°C differentiation
631 medium was exchanged. On day 8 attached BMDMs were detached using Accutase® (Innovative Cell
632 Technologies, Inc.), washed twice in PBS, counted, and used in the phagocytosis assay.

633 *Anti-ASC antibody cloning*

634 The anti-ASC antibody was cloned from B-cells of rabbits immunized with recombinant ASC (**Fig. 4B**).
635 Isotype control antibody is a similarly obtained anti-idiotypic rabbit monoclonal antibody isolated from
636 a rabbit immunized with a human IgG1 Fab. Recombinant antibodies were produced in a transient HEK
637 expression system and purified via protein A affinity purification on an automated AKTA system (AKTA
638 explorer FPLC, GE Healthcare). For *in vivo* studies rabbit V-regions were fused with murine constant of
639 mouse IgG2a heavy chain and kappa chain to minimize immunogenicity. Recombinant antibodies were
640 produced as described above but in addition remaining endotoxin was removed by hydrophobic
641 interaction chromatography (AKTA explorer FPLC, GE Healthcare). Endotoxin levels were measured
642 (Endosafe nexgen, Charles River) and only antibodies with less than 0.15 EU/mg were used for *in*
643 *vivo* studies.

644 *Anti-murine ASC antibody binding assay*

645 High-binding clear flat bottom 384-well plate (Huber lab) were coated o/n (4°C) with 10 µl/well of
646 murine ASC (Cusabio, CSB-EP861664 MO) at a concentration of 1.25 µg/ml or BSA at a concentration
647 of 1 µg/ml diluted in PBS. After o/n incubation, wells were aspirated and washed once with 100 µl/well
648 of wash buffer (0.05% Tween®20 in PBS). Wells were blocked for an hour with 50 µl of 2% BSA diluted
649 in PBS at RT. After blocking, wells were incubated 2 hours at RT with 10 µl of test antibody (anti-ASC
650 or isotype ctrl) and serially diluted. Wells were washed four times and consecutively incubated with
651 10 µl/well of detection antibody for an hour at RT. Unbound detection antibody was removed by

652 washing four times, and the wells were incubated with 20 µl TMB for 5 min. The reaction was stopped
653 by adding 10 µl of 1 M H_2SO_4 per well. Absorbance was immediately read at 450 nm.
654 *Anti-ASC antibody serum concentration measurements*
655 Serum was isolated as previously described. 384-well SpectraPlate HB plate was coated with
656 recombinant ASC-his at a concentration of 1 µg/ml in PBS (pH 7.4) and incubated o/n (4°C) with 20
657 µl/well. Plates were then washed three times with sample buffer (0.1% Tween®20 in PBS) and blocked
658 with blocking buffer (5 % SureBlockTM (Lubio Science, #SB232010-250G) in sample buffer) for 90 min
659 at RT. Blocking buffer was removed by plate flipping. Murine serum samples as well as positive (anti-
660 ASC monoclonal ab, Mabylon AG) and negative (isotype control ab, Mabylon AG) assay controls were
661 resuspended in sample buffer followed by serial dilution and incubation for 2 hours at 37°C. Starting
662 concentration of anti-ASC mAb was 2 µg/ml. Starting dilution of mouse serum samples was 1:20. After
663 four wash cycles, HRP-conjugated secondary antibody (Goat anti-mouse IgG (H+L), Jackson
664 ImmunoResearch, #115-035-003) were incubated for 1 h, at RT at a dilution of 1:4000 (in sample
665 buffer). After three wash cycles, plate was developed with 20 µl/well TMB and incubated for 5 min at
666 RT in the dark. Reaction was stopped with 20 µl/well 0.5 M H_2SO_4. Finally, absorbance was read at λ =
667 450 nm using an EnVision plate reader (Perkin Elmer). Serum samples as well as controls were assayed
668 in technical duplicates.
669 *In vitro phagocytosis*
670 The phagocytosis of BMDMs was performed using a phagocytosis assay kit (abcam). Individual samples
671 were prepared in duplicates. The in *vitro* assay was performed in 96-well tissue culture plates (TPP).
672 *Pycard*$^{+/+}$ and *Pycard*$^{-/-}$ BMDMs were suspended at a density of 500'000 cells/ml. BMDMs were
673 stimulated, with slight modifications, as previously published [23]. BMDMs were stimulated with murine
674 SAA1 at a concentration of 2 µg/ml for 16 hours at 37°C prior to phagocytosis substrate encounter.
675 After 1-hour phagocytosis substrate incubation at 37°C, cells were treated according to the
676 manufacturer's guidelines and proceeded to EnVision Multimode Plate Reader (PerkinElmer) for data
677 acquisition. The absorbance was determined at 405 nm.

678 *Assessment of cellular spleen composition by flow cytometry*

679 After sacrifice, cells were isolated from spleens using a 70 µm cell strainer (Falcon®). Following red
680 blood cell lysis, cells were stained with the following monoclonal antibodies to determine cellular
681 architecture of most abundant spleen and immune cells (**Table S10**): anti-mouse CD45.2 (Biolegend),
682 anti-mouse Gr-1 (eBioscience), anti-mouse F4/80 (eBioscience), anti-mouse CD11b (Biolgegend), anti-
683 mouse B220 (Biolegend), anti-mouse CD3 (Biolegend), anti-mouse CD206 (Biolegend), anti-mouse
684 MHCII (Biolegend) and anti-mouse CD11b (eBioscience). Data acquisition and analysis was performed
685 on a BD LSRIIFortessa™ flow cytometer and FlowJo v10.6.1, respectively. Gating strategy was applied,
686 with slight modifications, as previously published [72-74].

687 *RNA extraction and high-throughput sequencing (NGS)*

688 Upon flow cytometric sorting of F4/80+/CD11b+ splenic macrophages originating from AA^+ mice (see
689 above) total RNA was extracted using TRIzol™ Reagent (ThermoFisher Scientific) according to the
690 manufacturer's guidelines and proceeded to high throughput sequencing (NGS). RNA integrity and
691 quantity were assessed by RNA ScreenTape Analysis (Agilent). The SMARTer Stranded Total RNA-Seq
692 Kit- Pico Input Mammalian (Takara) together with a NovaSeq platform (Illumina) was applied for
693 transcriptomic data acquisition. Data was analyzed using established analysis pipelines at the
694 Functional Genomics Center Zurich (FGCZ).

695 *Complete blood count (CBC) from peripheral blood*

696 Blood was withdrawn into Microvette® 100 K3E (SARSTEDT Germany) cuvettes according to the
697 manufacturer's guidelines. To assess CBCs, samples were run on an ADVIA (Siemens Healthineers)
698 hematology system.

699 *Experimentation with human samples*

700 All experiments and analyses involving samples from human donors were conducted with the approval
701 of the ethics committee of the Canton Zurich (KEK-ZH-Nr. 2015-0561, BASEC-Nr. 2018-01042, and
702 BASEC-Nr. 2022-00293) and in accordance with the provisions of the Declaration of Helsinki and the
703 Good Clinical Practice guidelines of the International Conference on Harmonization.

704 *High-throughput antibody profiling in unselected patient cohort and validation experiments*

705 Serological screens were conducted as shown [50, 75, 76]. Briefly, high-binding 1536-well plates (Perkin
706 Elmer, SpectraPlate 1536 HB) were coated with 1 µg/ml human ASC protein containing a C-terminal
707 his-tag in PBS at 37 °C for 1 h, followed by three washes with PBS-T and by blocking with 5% milk in
708 PBS-T for 1.5 h. Three microliter plasma, diluted in 57 µl sample buffer (1% milk in PBS-T), were
709 dispensed at various volumes into human ASC-coated 1,536-well plates using contactless dispensing
710 with an ECHO 555 Acoustic Dispenser (Labcyte). Thereby, dilution curves ranging from plasma dilutions
711 1:50 to 1:6,000 were generated (eight dilution points per patient plasma sample). After the sample
712 incubation for 2 hours at RT, the wells were washed five times with wash buffer and the presence of
713 IgGs bound to ASC were detected using an HRP-linked anti-human IgG antibody (Peroxidase AffiniPure
714 Goat Anti-Human IgG, Fcγ Fragment Specific, Jackson, 109-035-098, at 1:4,000 dilution in sample
715 buffer). The incubation of the secondary antibody for one hour at RT was followed by three washes
716 with PBS-T, the addition of TMB, an incubation of three minutes at RT, and the addition of 0.5 M H_2SO_4.
717 The well volume for each step reached a final of 3 µl. The plates were centrifuged after all dispensing
718 steps, except for the addition of TMB. The absorbance at 450 nm was measured in a plate reader
719 (Perkin Elmer, EnVision) and the inflection points of the sigmoidal binding curves were determined
720 using a custom designed fitting algorithm. Samples reaching half-maximum saturation (shown as the
721 inflection point of the logistic regression curve) at a concentration ≤ 1:100, i.e., at $p(EC_{50}) \geq 2$, and with
722 a mean squared residual error < 20% of the actual $p(EC_{50})$ were considered hits. The inclusion of a
723 threshold for fitting error ensures a reliable identification of positives from high-throughput screening.
724 Negative $p(EC_{50})$ values, reflecting nonreactive samples, were rescaled as zero.

725 For the validation screen, hits from the high-throughput screen were tested against a panel of antigens
726 consisting of recombinant human ASC protein, human $recPrP_{23-230}$, the full-length tau protein (Tau441),
727 the SARS-CoV-2 Spike ectodomain and natural Ara h 2 allergen. The validation screen was performed
728 identically to the primary high-throughput screen, except that duplicates were used instead of unicates
729 and a 384-well plate format was chosen. Samples from the validation screen were considered

730 confirmed if p(EC_{50}) for PrP ≥ 2 (distinct reactivity against ASC) and p(EC_{50}) for other targets < 2 (no
731 distinct reactivity against any other control target), except for the SARS-CoV-2 Spike protein, which
732 was included to assess potential associations with acute infection or vaccination. The following assay
733 positive controls were used at a starting concentration of 1 µg/ml: (1) Anti-ASC/TMS1/PYCARD
734 Antibody (B-3) mouse monoclonal IgG1 (sc-514414, Santa Cruz); (2) anti-human PrP antibody huPOM1
735 [50]; (3) Anti-Tau (4-repeat isoform RD4) Antibody, clone 1E1/A6 (05-804, Sigma-Aldrich). Additional
736 assay positive controls used at a starting dilution of 1:50 were: a plasma pool of patients admitted to
737 the University Hospital of Zurich due to COVID-19 (anti-Spike PC); plasma of a patient identified to be
738 seropositive for IgG against nAra h 2 (anti-Ara h 2 PC). The experiment on the two ASC domains (PYD
739 and CARD, both of them containing a C-terminal his-tag; produced by Mabylon AG, Schlieren) and on
740 additional his-tagged proteins as controls (his-LAG3 [77], his-TIM3 (AcroBiosystems)) was conducted
741 using the same ELISA protocols as outlined above. Antigens and antibodies used for the high-
742 throughput antibody profiling are shown in **Table S11** and **S12**.

743 *Statistical analysis*

744 Statistical analysis was performed using GraphPad Prism v9, Python3 and R. If not indicated otherwise,
745 we conducted Kruskal-Wallis test with post-hoc Wilcoxon rank sum test with Holms correction for
746 multiple comparison on non-parametric data. Statistical details are described in the respective figure
747 legends and in the Result section. A two-tailed *p*-value <0.05 was considered as statistically significant
748 in all group-based experiments, except for the exploratory ICD-10 code-based analysis where the
749 significant threshold, α, was 0.01. Confidence intervals were calculated at a confidence level of 95 %.
750 When reporting medians, we usually provided the interquartile range (IQR). Human data are stored in
751 an *MS-SQL* database. Multiple regression with a logit link function using various p(EC_{50}) cutoff values
752 for ICD-10 data exploration was performed using the rstanarm package (https://mc-
753 stan.org/rstanarm/) with a Bayesian LASSO prior, similar to what was expounded in detail previously
754 [53, 54].

755

Acknowledgments

We appreciate that Dr. Emmanuel Contassot shared the B6.129-*Pycard*^{tm1Vmd} mice. We thank Dr. Marcus Fändrich and his colleagues for providing murine SAA1 protein. We are grateful that Dr. Itzel Condado-Morales and Dr. Sathish Kumar provided technical support with the aggregation assay and data analysis. We thank Dr. Markus Manz that we could use the ADVIA hematology system. We thank Inga Hochheiser and Dr. Matthias Geyer (ISB, University of Bonn, Germany) for providing the human ASC and the team of Mabylon AG (Schlieren) for sharing the ASC-PYD and the ASC-CARD proteins. We thank Petra Schwarz, Rita Moos, Jingjing Guo, Mirzet Delic and Paulina Pawlak for their valuable technical knowledge, advice and assistance in mouse breeding and experimental injections. We thank the histology team at the institute for neuropathology for their support. We thank the RNA sequencing core from the University of Zurich for their help in the data analysis. The high-throughput antibody profiling-related work was funded through an SPHN driver grant (2017DRI1) and through NOMIS Foundation, the Schwyzer Winiker Stiftung, and the Baugarten Stiftung (coordinated by the USZ Foundation, USZF27101) awarded to AA and ME. AA is supported by the Swiss National Science Foundation (grant # 179040) and the NOMIS Foundation.

Statement of author contribution

Initiated, conceptualization and lead the project: ML, AA. Conceived and designed the experiments: ML. Supervised the project: AA. Wrote the ethical applications to perform the animal experiments: ML, AKKL. Wrote the ethical applications to perform experiments with human samples or data: ME, RRR. Animal breeding and genotyping: ML. Performed *in vivo* experiments: ML, PMS. Anti-ASC antibody cloning, expression, and purification: NP, DC, DB. Animal injections: ML. Performed the *in vitro* as well as human HTS confirmatory experiments: ML, ME, TS, SH. Bulk RNA isolation: ML, MC. Isolated and purified murine AEF: GTW. Synthetized and purified LCP: KPRN. Histology: ML, PDR, ME. Provided human autopsy material: NJR. Contributed reagents and materials: KJF, MN. Flow cytometry and FACS experiments: ML, VL, PMS. Analysis and visualization of the data: ML, ME, PDR, PMS. Conducted the

population-wide anti-ASC autoantibody screen and profiling: ME. Wrote the original draft of the manuscript: ML, ME. Edited manuscript: ML, ME, PDR, AA, PMS, NP, TS. Approved manuscript: all authors.

Data and material statement

Primary data and reagents will be shared and made available upon request. Antibodies against ASC are the property of Mabylon AG and will be shared upon reasonable request under specific material transfer agreement terms.

Declaration of interests

AA is a founder, shareholder, director, and consultant for Mabylon AG, which has developed the anti-ASC monoclonal antibody used in this study. NP, DC, DB are employees of Mabylon AG.

Supplemental figures

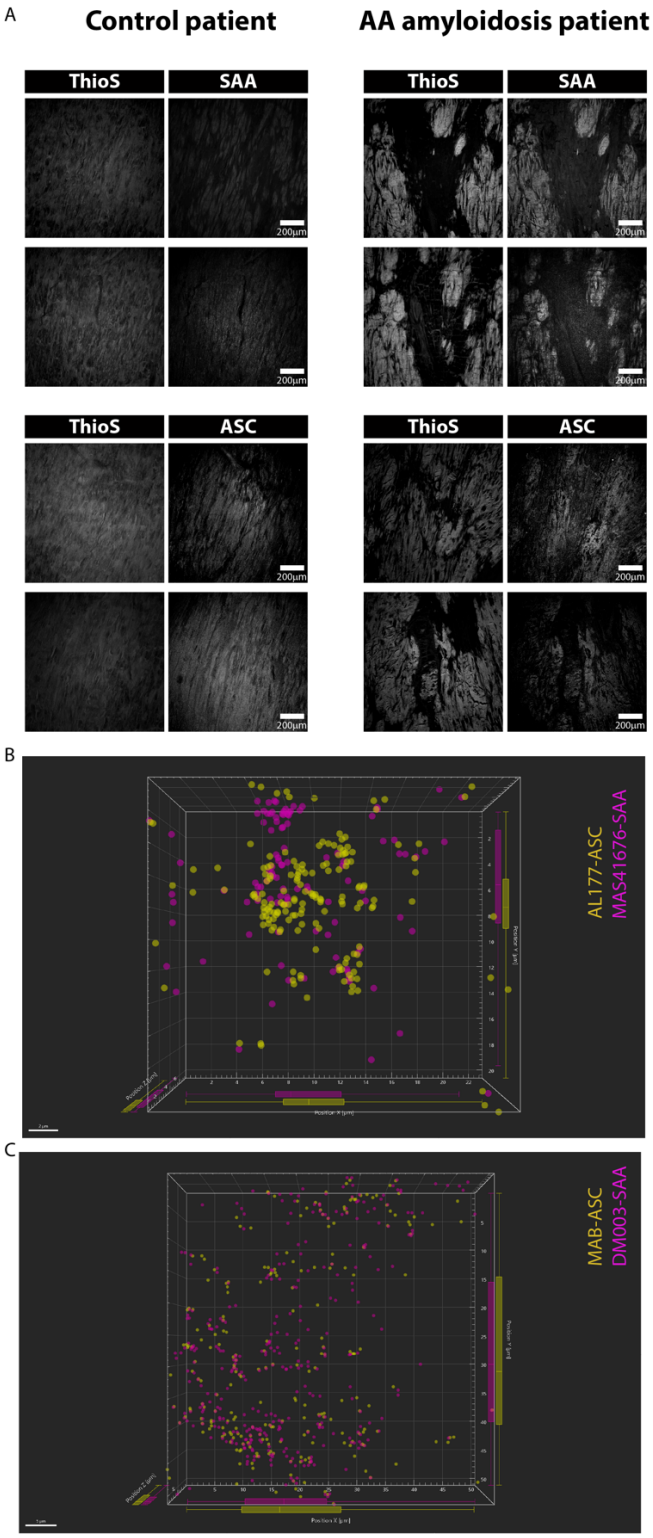

Fig. S1. Colocalization of Thioflavin S staining with ASC and SAA and 3D representation of ASC and SAA staining. (A) Confocal images of patient with or without AA amyloidosis showing Thioflavin S staining, revealing protein aggregates forming β-sheets, and SAA or ASC. All grey levels were adjusted identically for both subjects. **(B)** and **(C)** Plot presenting 3D geolocalisation of center of mass of the dots reconstructed on the STED signal for ASC and SAA. On the side, boxplots represent the distribution in X, Y, and Z direction. The distributions of ASC and SAA are highly congruent.

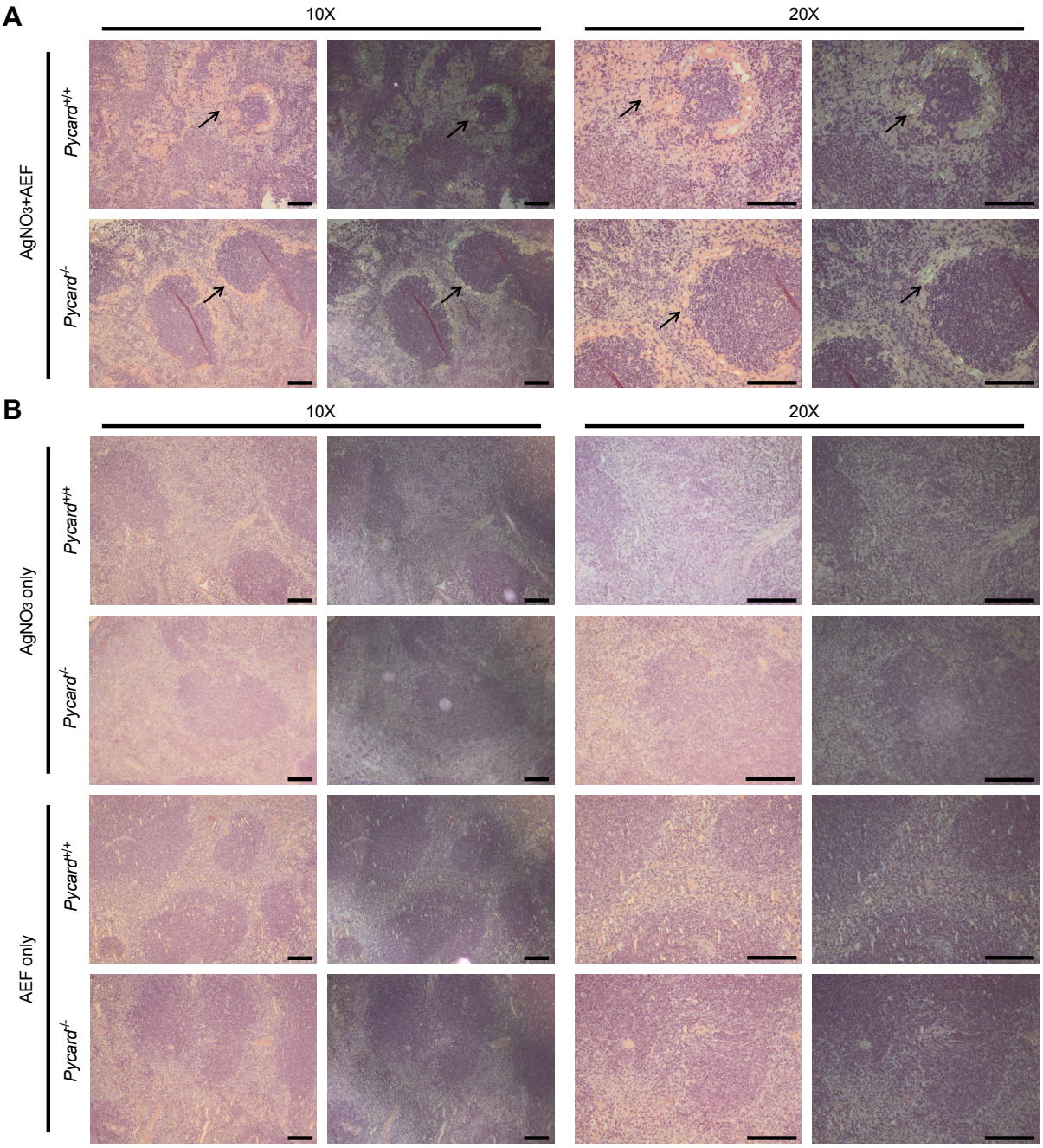

802

803 **Fig. S2**. **Amyloid stained by Congo red shows apple-green birefringence in polarized light only in mice with AA induction**.
804 **(A)** Representative Congo red-stained photo micrographs from indicated experimental groups showing amyloid apple-green
805 birefringence (black arrows) under polarized light in AA^+ mice that received both, AEF and $AgNO_3$ injections [78]. In light
806 microscopy, amyloid manifests as amorphous pink material (black arrows). **(B)** Important to note, there is no amyloid in the
807 $AgNO_3$ only nor in the AEF only treated group (AA^- mice). Scale bar 100 µm.

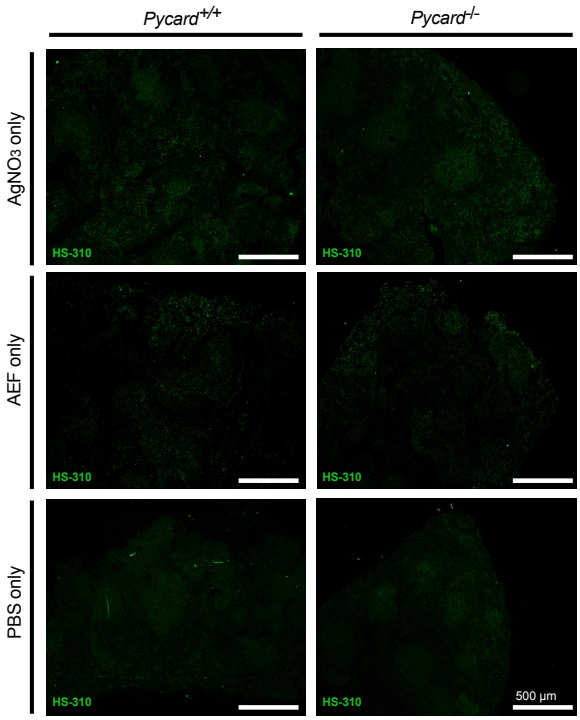

808

809 **Fig. S3**. **Absence of amyloid deposition in mice only treated with $AgNO_3$, AEF or PBS (AA^- mice)**. Visualization of amyloid
810 deposition by hexameric LCP HS-310. No amyloid was seen in the control groups ($AgNO_3$-only, AEF-only and PBS-only). Light
811 exposure time and 4x microscope objective were kept equal throughout the imaging/experiment.

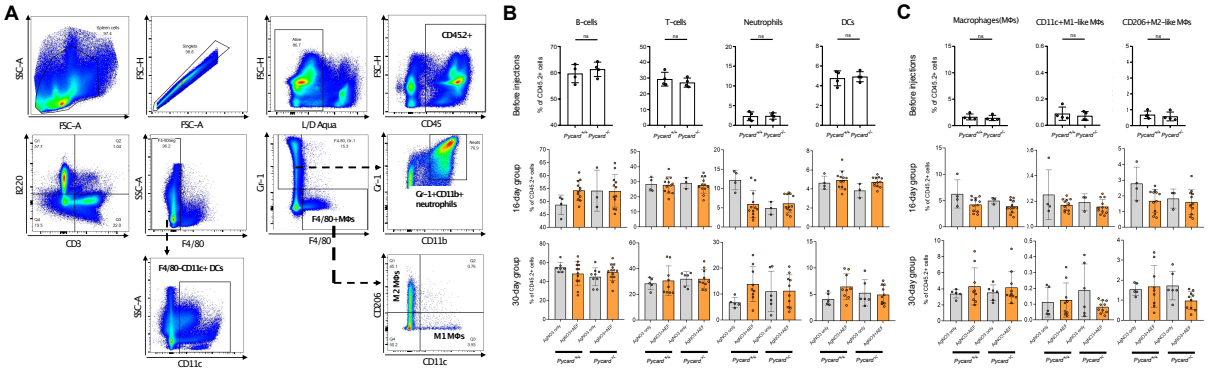

Fig. S4. **Assessment of splenic cellular architecture before injections and AA disease state**. **(A)** Representative flow cytometry analysis and gating strategy of murine spleen cells. CD45.2 is an alloantigen expressed on all hematopoietic cells (except mature erythrocytes and platelets). B cells defined as CD45+CD3-B220+, T cells defined as CD45+B220-CD3+, Dendritic cells (DCs) defined as CD45+F4/80-CD11c+ and Neutrophils defined as CD45+Gr-1+CD11b+. Macrophages (MΦs) defined as CD45+F4/80+, and M1-like MΦs defined as CD45+F4/80+CD206-CD11c+ whereas M2-like MΦs defined as CD45+F4/80+CD11c-CD206+. **(B)** Relative abundance of B cells, T cells, neutrophils and dendritic cells (DCs) are plotted as percentage of CD45.2 positive events. Three different time points are represented. First row of panels: Before injections. Second row of panels: 16-days group. Third row of panels: 30-days group. There is no statistically significant difference in splenic cellular composition in unpaired two-tailed Student's t-test between the equivalent experimental group of *Pycard*$^{+/+}$and *Pycard*$^{-/-}$ mice at each individual time point. Error bar represents standard error of the mean (SEM). Each dot represents an individual mouse. **(C)** F4/80+ macrophages, M1-like MΦs and M2-like MΦs are plotted as percentage of CD45.2 positive events at three different time points. First lane panel represents baseline values whereas data of animals euthanized after 16 and 30 days are plotted in the second and third lane panels, respectively. ⁻ . Results are represented as mean ± standard error. Each dot represents one individual mouse.

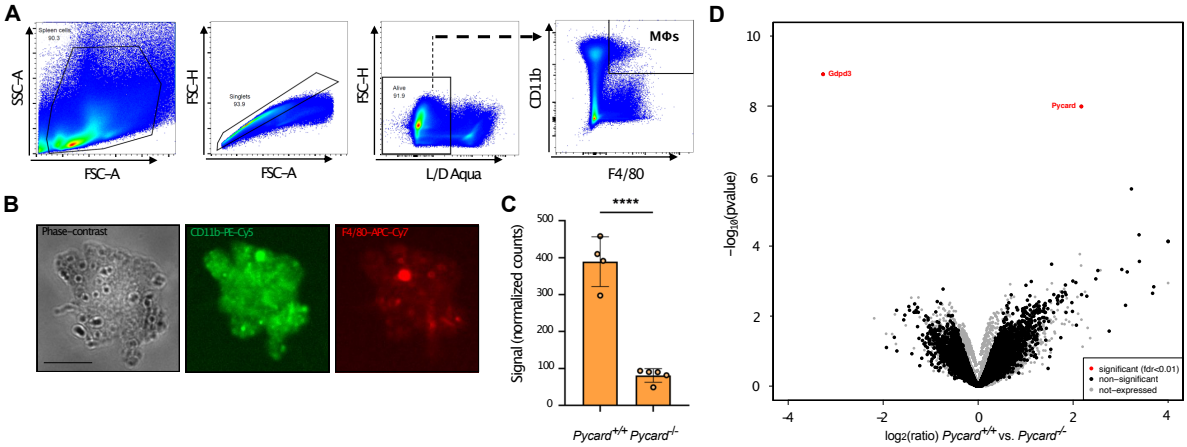

Fig. S5. **Transcriptional analysis of splenic macrophages from AA⁺ mice reveals mainly changes in *Pycard* expression**. **(A)** Representative gating strategy of splenic macrophages flow cytometrically sorted from AA⁺ mice. Splenic cells were first gated in an FSC-A vs. SSC-A plot followed by doublet and dead cell exclusion. Finally, CD11b+F4/80+ macrophages were bulk sorted for transcriptomic analysis. **(B)** Representative images of splenic macrophages assessed **by** phase contrast and fluorescence microscopy. . The middle and right panel confirms the presence of the two antibody-conjugated fluorophores PE-Cy5 and APC-Cy7 that were used to identify CD11b+ and F4/80+ macrophages, respectively. Scale bar: approximately 10 µm. **(C)** Scatter plot depicting normalized counts of ASC transcript reads. An unpaired, two-tailed Students' t-tests was performed. Each dot represents one individual mouse. **(D)** 'Volcano plot' of statistical significance vs. foldchange between *Pycard*$^{+/+}$and *Pycard*$^{-/-}$ splenic macrophages from AA⁺ mice displays the most significantly and differentially expressed genes (in red). * $P<0.05$, **** $P<0.0001$, ns: not significant.

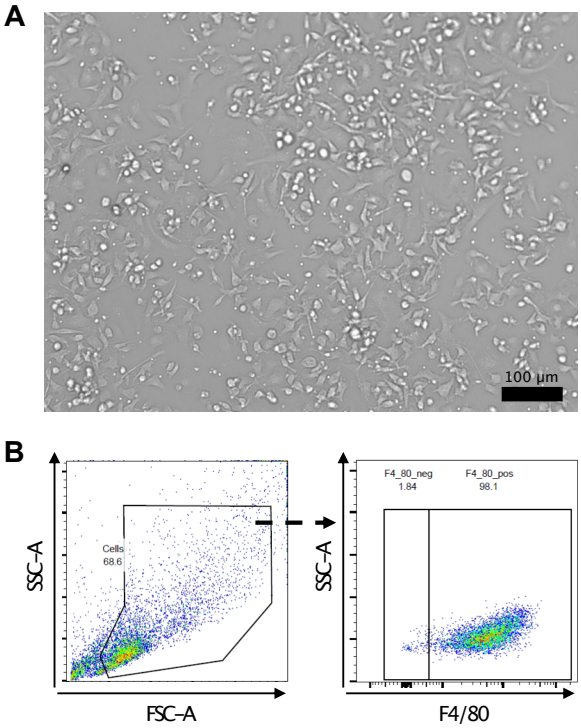

838

839 **Fig. S6**. ***In vitro* phagocytosis of SAA-stimulated BMDMs**. **(A)** Phase contrast micrograph of adherent and differentiated
840 BMDMs. **(B) Representative** flow cytometry gating for BMDM differentiation performed with anti-mouse F4/80 antibody, a
841 specific macrophage marker. Alive (not shown) F4/80+ cells represent differentiated BMDMs.

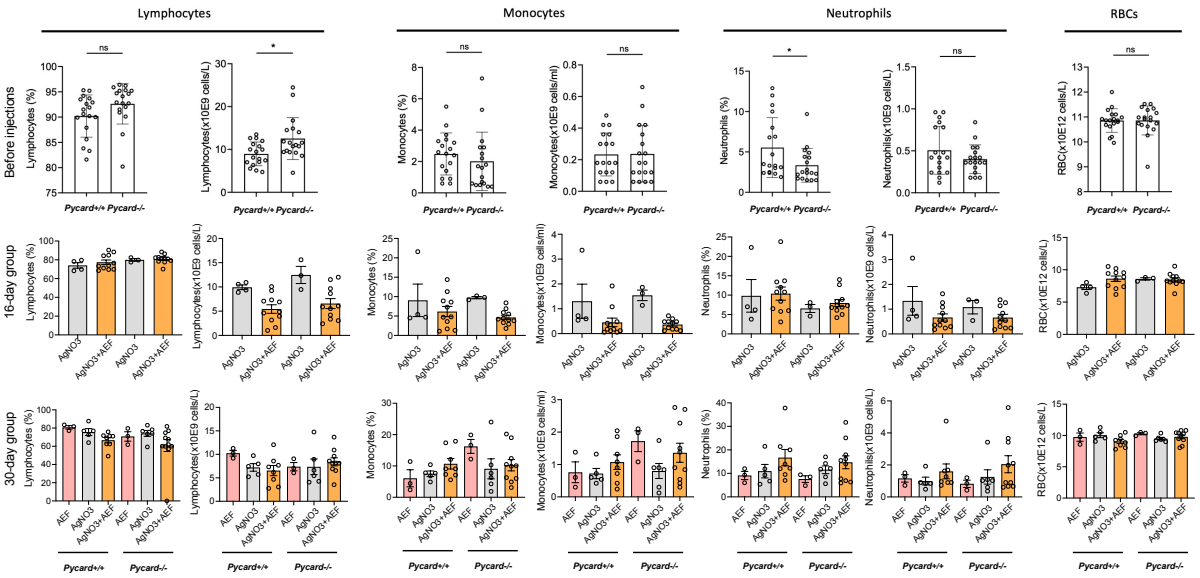

Fig. S7. **Complete blood count (CBC) assessment did not reveal significant changes in cellular blood compartments between AA-diseased and $AgNO_3$-only control animals**. Bar plots depicting the abundance of lymphocytes, monocytes, neutrophils red blood cells (RBCs) plotted in relative (%) as well as absolute values (cell numbers). Top panel represents before injections values of *Pycard*$^{+/+}$and *Pycard*$^{-/-}$ mice. Data of mice euthanized at day 16 and 30 are plotted in the middle and bottom panels, respectively. Results are represented as mean± standard deviation and SEM (error bars). Statistical analysis performed by unpaired two-tailed Student's t-test in CBC between the equivalent experimental group. Each dot represents one individual mouse. * $P<0.05$, ns: not significant.

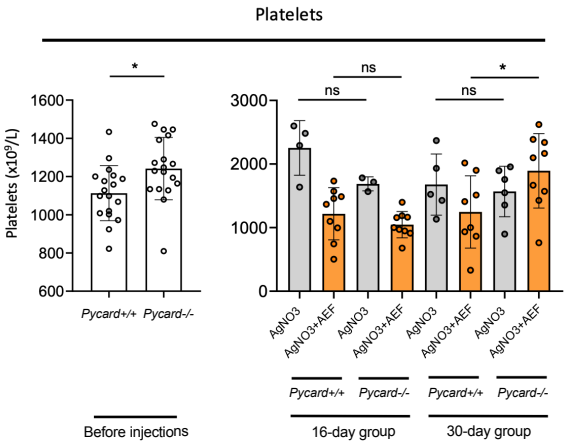

Fig. S8. **Altered platelet count in the absence of *Pycard* before injections and in AA disease state**. Bar plots depicting platelet counts from experimental mice and different time points are represented. Results are represented as mean± standard deviation (error bars). Platelet counts < 150 x10^9/L were excluded from analysis. Analysis was performed using unpaired two-tailed Student's t-tests. Each dot represents one individual mouse. * *P*<0.05, ns: not significant.

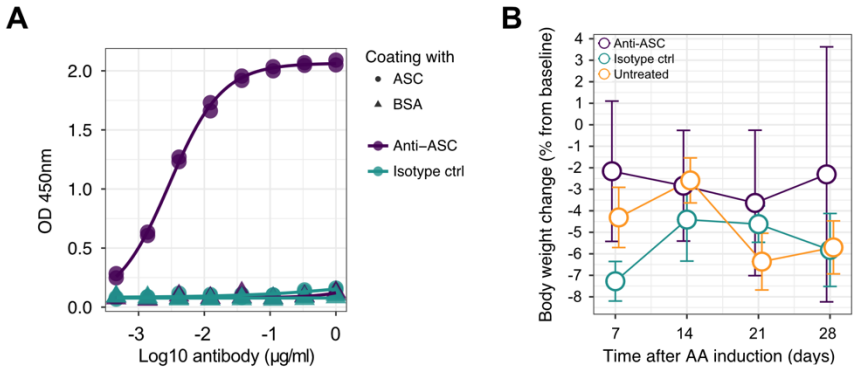

855

856 **Fig. S9**. **Anti-ASC antibody binding curve and body weight changes during immunotherapy. (A)** ASC-specific binding assay
857 for custom ASC and isotope control antibody. **(B)** Body weight change during the experiment (± SEM). Groups of 3 animals
858 were treated with anti-ASC antibodies, isotype control, or were left untreated. Statistics: Kruskal-Wallis test.

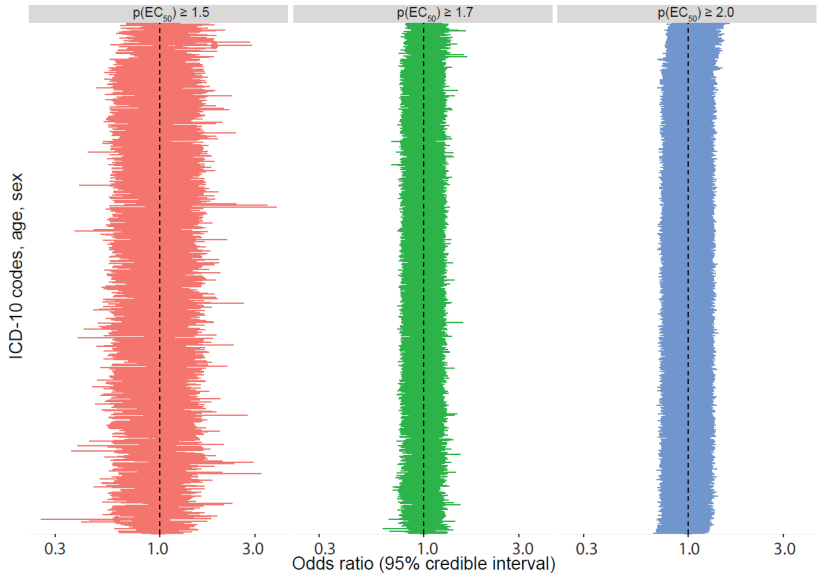

Fig. S10. **Sensitivity analysis of different p(EC_{50}) cutoff values using multiple logisitc regression analysis**. Different p(EC_{50}) cutoff values that range from 1.5 (left), 1.7 (middle) to 2.0 (right). Y-axis: ICD-10 codes, age, and sex, which have been subjected to multiple logistic regression analysis using a Bayesian LASSO prior. X-axis: Odds ratio (OR) with 95% credible interval.

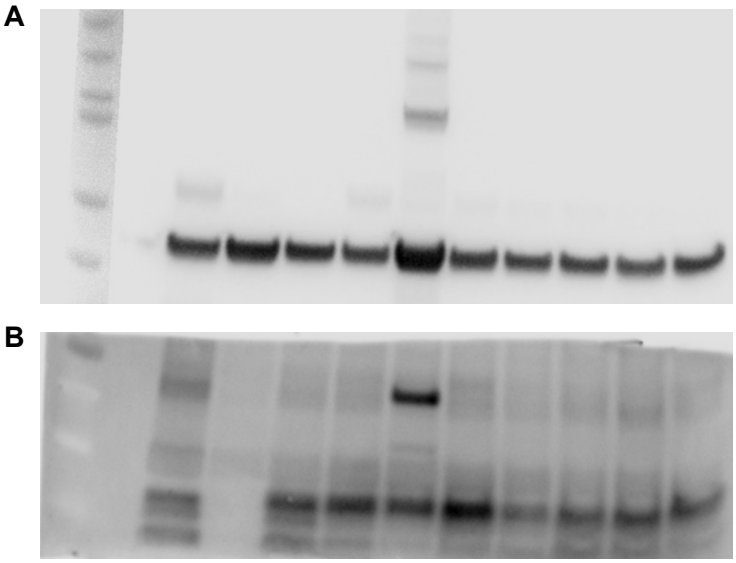

Fig. S11. **Uncropped and unmodified western blot images of Fig. 3**. **(A)** Uncropped image of western blot that was performed on spleen homogenate of AA^+ mice and probed with anti-actin primary antibody. **(B)** Uncropped image of western blot that was performed on spleen homogenate of AA^+ mice and probed with anti-SAA primary antibody for SAA detection. Of important note, the upper main band visible in lane 5 most likely represents an oligomeric SAA species.

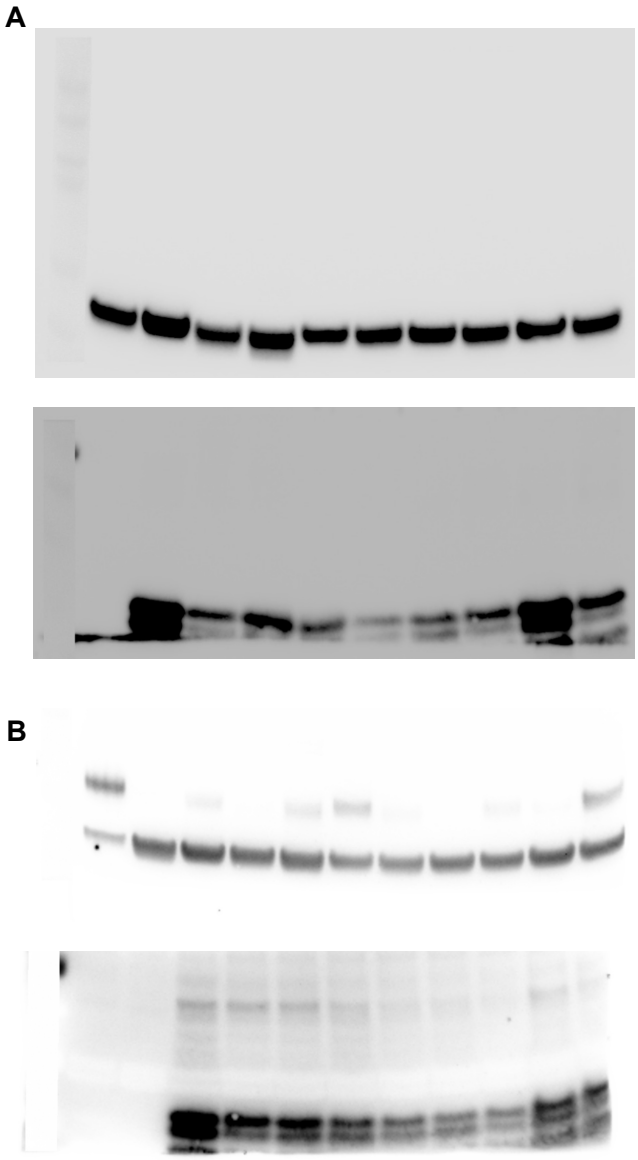

Fig. S12. **Uncropped Western blot images of Fig. 4**. **(A)** Uncropped image of Western blot that was performed on spleen homogenate of AA^+ mice and probed with anti-actin primary antibody (upper blot). Uncropped image of Western blot that was performed on spleen homogenate of AA^+ mice and probed with anti-SAA primary antibody for SAA detection (lower blot). **(B)** Second representative Western blot. Uncropped image of Western blot that was performed on spleen homogenate of AA^+ mice and probed with anti-actin primary antibody (upper blot). Uncropped image of Western blot that was performed on spleen homogenate of AA^+ mice and probed with anti-SAA primary antibody for SAA detection (lower blot). Of note: Small part of the membrane (last lane in the lower blot) was cut during processing.

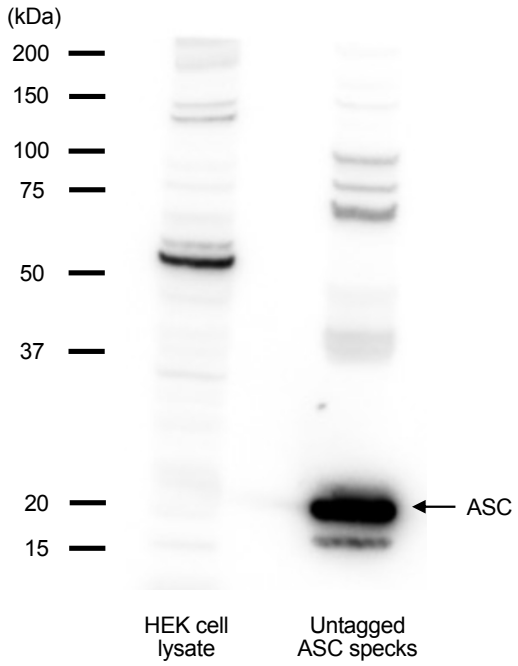

878

879 **Fig. S13. Purified ASC speck assessment by western blot**. Uncropped image of western blot that was performed on HEK cell
880 lysate (control, left lane) and purified untagged ASC specks (right lane) and probed with anti-ASC primary antibody for ASC
881 detection and assessment. Different bands and respective sized in the right lane represent ASC oligomers.

882 Supplemental tables

883 *Table S1. Accelerated SAA fibrillation in the presence of ASC specks.*

ASC specks (nr #) / Time ($t_{1/2}$)	0	1×10^5	2×10^5	5×10^5
Mean ± SD (hours)	98.83 ± 8.16	82.12 ± 8.73	79.22 ± 7.18	66.30 ± 4.10

884

885 *Table S2. Temporal SAA serum concentrations upon silver nitrate injection or AA induction.*

	Pycard$^{+/+}$		*Pycard*$^{-/-}$	
Group / Time (hrs)	$AgNO_3$ Mean ± SD (µg/ml)	$AgNO_3$+AEF Mean ± SD (µg/ml)	$AgNO_3$ Mean ± SD (µg/ml)	$AgNO_3$+AEF Mean ± SD (µg/ml)
Baseline	6.08 ± 6.44	1.49 ± 1.22	1.39 ± 0.99	1.27 ± 1.06
9h	84.44 ± 15.22	63.41 ± 36.12	49.08 ± 38.48	80.98 ± 49.2
24h	217.1 ± 124.5	125.4 ± 25.04	188.5 ± 120	231.9 ± 97.13
48h	118 ± 60.21	95.2 ± 40.01	106.5 ± 65.24	149 ± 34.62
72h	19.22 ± 10.65	16 ± 5.94	16.16 ± 7.7	26.69 ± 10.79
96h	3.28 ± 0.47	3.48 ± 1.55	4.38 ± 0.79	7.04 ± 5.77

886

887 *Table S3. HS-310-stained AA amyloid.*

	Pycard$^{+/+}$		*Pycard*$^{-/-}$	
Treatment / Group	$AgNO_3$ Mean ± SD (HS-310 area, %)	$AgNO_3$+AEF Mean ± SD (HS-310 area, %)	$AgNO_3$ Mean ± SD (HS-310 area, %)	$AgNO_3$+AEF Mean ± SD (HS-310 area, %)
16- day	-	6.13 ± 4.48	-	3.11 ± 2.46
30-day	-	17.63 ± 8.38	-	8.93 ± 6.5

888 *Table S4. Phagocytosis of Pycard$^{+/+}$ and Pycard$^{-/-}$ BMDMs.*

Genotype / Condition BMDMs	*Pycard*$^{+/+}$ Mean ± SD OD at 405 nm	*Pycard*$^{-/-}$ Mean ± SD OD at 405 nm	*p*-value	Sign.
Unstimulated	1.58 ± 0.03	1.53 ± 0.09	0.393	ns
Unstimulated + Cytochalasin D	0.32 ± 0.03	0.35 ± 0.03	0.077	ns
mSAA stimulated	1.72 ± 0.05	1.55 ± 0.11	0.002	sign.
mSAA stimulated + Cytochalasin D	0.34 ± 0.05	0.34 ± 0.01	0.630	ns

889

890 *Table S5. Genotype and sex of experimental animals.*

Group / Gender	AEF+$AgNO_3$ 16- and 30-day group	$AgNO_3$ only 16- and 30-day group	PBS only	AEF only	Total (n =)
Pycard$^{-/-}$ females (n =)	10	4	3	1	18
Pycard$^{-/-}$ males (n =)	14	6	0	3	23
Pycard$^{+/+}$ females (n =)	10	4	0	0	14
Pycard$^{+/+}$ males (n =)	12	6	3	3	24
Total (n =)	46	20	6	7	79

891

892 *Table S6. Genotype and age of experimental animals.*

Genotype / Treatment	*Pycard*$^{+/+}$	*Pycard*$^{-/-}$	*p*-value	Sign.
PBS-only (mean days ± SD)	77.67 ± 1.16	58.33 ± 19.63	0.164	ns
AEF-only (mean days ± SD)	80.33 ± 1.16	59.75 ± 15.17	0.071	ns
$AgNO_3$-only (mean days ± SD)	100.0 ± 20.07	94.8 ± 21.14	0.580	ns
$AgNO_3$ + AEF (mean days ± SD)	81.68 ± 12.11	88.96 ± 16.53	0.101	ns

Total (mean days ± SD)	86.08 ± 15.93	85.20 ± 21.18	0.837	ns

893

894 Table S7. Sex of experimental immunotherapy animals

Treatment / Gender	AEF+$AgNO_3$ (AA induction)	AA + anti-ASC abs	AA + isotype abs	Total (n =)
Pycard$^{+/+}$ females (n =)	4	3	4	11
Pycard$^{+/+}$ males (n =)	1	2	1	4
Total (n =)	5	5	5	15

895

896 *Table S8. Age of experimental immunotherapy animals.*

Genotype / Treatment	*Pycard*$^{+/+}$	*p*-value	Sign.
1.) AA induction only (mean weeks ± SD)	19.8 ± 5.59	1 vs 2: 0.959	ns
2.) AA + anti-ASC abs (mean weeks ± SD)	18.8 ± 4.76	2 vs 3: 0.974	ns
3.) AA + isotype abs (mean weeks ± SD)	19.6 ± 6.73	3 vs 1: 0.998	ns
Total (mean weeks ± SD)	19.4 ± 5.34	0.959	ns

897

898 Table S9. Western blot antibodies.

Antibody	Clone	Host / Conjugate	Source	Dilution (µl)
SAA recombinant rabbit monoclonal	D9H4L41	Rabbit	Invitrogen, #700830	1:200
Goat anti-rabbit IgG (H+L)	-	Goat/ HRP	Jackson Immuno, #111-035-045	1:5000
Anti-Actin antibody monoclonal	C4	Mouse	Merck, #MAB1501R	1:8000

Goat anti-mouse IgG (H+L)	-	Goat/ HRP	Jackson Immuno, #115-035-003	1:8000

899

900 Table S10. Flow cytometry antibodies.

Surface antigen	Fluorophore	Source	Dilution (µl)
Anti-mouse B220	Brilliant Violet 785	Biolegend, #103245	1:400
Anti-mouse CD11b	Brilliant Violet 650	Biolegend, #101239	1:400
Anti-mouse CD45.2	Pacific Blue	Biolegend, #109820	1:100
Anti-mouse CD3	Per/CPCy5.5	Biolegend, #100218	1:100
Anti-mouse Gr-1	PE/Cy5	eBioscience™, #15-5931-82	1:400
Anti-mouse CD206	PE	Biolegend, #141705	1:100
Anti-mouse F4/80	APC-eFluor 780	eBioscience™, #47-4801-82	1:200
Anti-mouse MHCII	Alexa Fluor® 700	Biolegend, #107621	1:800
Anti-mouse CD11c	APC	eBioscience™, #17-0114-82	1:400

901

902 Table S11. Antigens used for the high-throughput antibody profiling.

Antigen	Application	Coating concentration	Source	Product #
ASC-C-his	ELISA	1 µg/ml	Matthias Geyer, ISB, University of Bonn [15]	
human recPrP$_{23-230}$	ELISA	1 µg/ml	In-house [50]	
Tau441	ELISA	2 µg/ml	In-house	
SARS-CoV-2 Spike ECD	ELISA	1 µg/ml	[75]	
nAra h 2	ELISA	1 µg/ml	Indoor Biotechnologies	NA-AH2-1
ASC-PYD	ELISA	1 µg/ml	Mabylon AG, Schlieren	

ASC-CARD	ELISA	1 µg/ml	Mabylon AG, Schlieren	
LAG3	ELISA	1 µg/ml	AcroBiosystems	LA3-H5222
TIM3	ELISA	1 µg/ml	AcroBiosystems	TM3-H5229

903

904 Table S12. Antibodies used for the high-throughput antibody profiling.

Species	Target	Dilution/Concentration range	Brand name	Product #
(HRP) Goat	anti-human IgG	1:4000	Jackson	109-035-098
(HRP) Goat	anti-mouse IgG	1:2000	Jackson	115-035-003
(HRP) Goat	anti-rabbit IgG	1:2000	Jackson	111-035-045
Mouse	anti-ASC	1 µg/ml - 0.06 ng/ml	Santa Cruz	sc-514414
Human	anti-human PrP	1 µg/ml - 0.06 ng/ml	In-house	
Mouse	anti-Tau441	1 µg/ml - 0.06 ng/ml	Sigma-Aldrich	05-804
Mouse	anti-his	1 µg/ml - 1,38 ng/ml	Invitrogen	37-2900
Rabbit	anti-ASC	1 µg/ml - 1,38 ng/ml	Mabylon AG, Schlieren	MY6745

905

References

1. Papa R, Lachmann HJ. Secondary, AA, Amyloidosis. Rheum Dis Clin North Am 2018;44:585-603.
2. Brunger AF, Nienhuis HLA, Bijzet J, et al. Causes of AA amyloidosis: a systematic review. Amyloid 2020;27:1-12.
3. Lee JY, Hall JA, Kroehling L, et al. Serum Amyloid A Proteins Induce Pathogenic Th17 Cells and Promote Inflammatory Disease. Cell 2020;180:79-91 e16.
4. Sack GH. Serum amyloid A - a review. Mol Med 2018;24:46.
5. Ye RD, Sun L. Emerging functions of serum amyloid A in inflammation. J Leukoc Biol 2015;98:923-9.
6. Westermark GT, Westermark P. Serum amyloid A and protein AA: molecular mechanisms of a transmissible amyloidosis. FEBS Lett 2009;583:2685-90.
7. Dubrey SW, Cha K, Simms RW, et al. Electrocardiography and Doppler echocardiography in secondary (AA) amyloidosis. Am J Cardiol 1996;77:313-5.
8. Chamling B, Drakos S, Bietenbeck M, et al. Diagnosis of Cardiac Involvement in Amyloid A Amyloidosis by Cardiovascular Magnetic Resonance Imaging. Front Cardiovasc Med 2021;8:757642.
9. Heneka MT, Kummer MP, Latz E. Innate immune activation in neurodegenerative disease. Nat Rev Immunol 2014;14:463-77.
10. Heneka MT, Golenbock DT, Latz E. Innate immunity in Alzheimer's disease. Nat Immunol 2015;16:229-36.
11. Anders HJ, Muruve DA. The inflammasomes in kidney disease. J Am Soc Nephrol 2011;22:1007-18.
12. Aguzzi A. The protean roles of neuroinflammation in trauma, infections, autoimmunity and neurodegeneration. Semin Immunol 2022;61-64:101655.
13. Jang S, Jang WY, Choi M, et al. Serum amyloid A1 is involved in amyloid plaque aggregation and memory decline in amyloid beta abundant condition. Transgenic Res 2019;28:499-508.
14. Ising C, Venegas C, Zhang S, et al. NLRP3 inflammasome activation drives tau pathology. Nature 2019;575:669-673.
15. Venegas C, Kumar S, Franklin BS, et al. Microglia-derived ASC specks cross-seed amyloid-β in Alzheimer's disease. Nature 2017;552:355-361.
16. Dansokho C, Heneka MT. Neuroinflammatory responses in Alzheimer's disease. J Neural Transm (Vienna) 2018;125:771-779.
17. Fernandes-Alnemri T, Alnemri ES. Assembly, purification, and assay of the activity of the ASC pyroptosome. Methods Enzymol 2008;442:251-70.
18. Eisenberg D, Jucker M. The amyloid state of proteins in human diseases. Cell 2012;148:1188-203.
19. Balci-Peynircioglu B, Waite AL, Schaner P, et al. Expression of ASC in renal tissues of familial mediterranean fever patients with amyloidosis: postulating a role for ASC in AA type amyloid deposition. Exp Biol Med (Maywood) 2008;233:1324-33.
20. Scarpioni R, Ricardi M, Albertazzi V. Secondary amyloidosis in autoinflammatory diseases and the role of inflammation in renal damage. World J Nephrol 2016;5:66-75.
21. Pastore S, Paloni G, Gattorno M, et al. PReS-FINAL-2240: Serum amyloid protein a concentration in CAPS patients treated with anti IL1B. Pediatric Rheumatology 2013;11:P230.
22. Niemi K, Teirilä L, Lappalainen J, et al. Serum amyloid A activates the NLRP3 inflammasome via P2X7 receptor and a cathepsin B-sensitive pathway. J Immunol 2011;186:6119-28.
23. Chen W, Qiang X, Wang Y, et al. Identification of tetranectin-targeting monoclonal antibodies to treat potentially lethal sepsis. Sci Transl Med 2020;12.
24. Gaiser AK, Bauer S, Ruez S, et al. Serum Amyloid A1 Induces Classically Activated Macrophages: A Role for Enhanced Fibril Formation. Front Immunol 2021;12:691155.
25. Lundmark K, Vahdat Shariatpanahi A, Westermark GT. Depletion of spleen macrophages delays AA amyloid development: a study performed in the rapid mouse model of AA amyloidosis. PLoS One 2013;8:e79104.
26. Sponarova J, Nuvolone M, Whicher C, et al. Efficient amyloid A clearance in the absence of immunoglobulins and complement factors. Am J Pathol 2013;182:1297-307.
27. Kisilevsky R, Boudreau L. Kinetics of amyloid deposition. I. The effects of amyloid-enhancing factor and splenectomy. Lab Invest 1983;48:53-9.
28. Magy N, Liepnieks JJ, Benson MD, et al. Amyloid-enhancing factor mediates amyloid formation on fibroblasts via a nidus/template mechanism. Arthritis Rheum 2003;48:1430-7.

29. Kennel SJ, Macy S, Wooliver C, et al. Phagocyte depletion inhibits AA amyloid accumulation in AEF-induced huIL-6 transgenic mice. Amyloid 2014;21:45-53.
30. Nyström SN, Westermark GT. AA-Amyloid is cleared by endogenous immunological mechanisms. Amyloid 2012;19:138-45.
31. Pepelnjak M, de Souza N, Picotti P. Detecting Protein-Small Molecule Interactions Using Limited Proteolysis-Mass Spectrometry (LiP-MS). Trends Biochem Sci 2020;45:919-920.
32. Schopper S, Kahraman A, Leuenberger P, et al. Measuring protein structural changes on a proteome-wide scale using limited proteolysis-coupled mass spectrometry. Nat Protoc 2017;12:2391-2410.
33. Schurch PM, Malinovska L, Hleihil M, et al. Calreticulin mutations affect its chaperone function and perturb the glycoproteome. Cell Rep 2022;41:111689.
34. Cappelletti V, Hauser T, Piazza I, et al. Dynamic 3D proteomes reveal protein functional alterations at high resolution in situ. Cell 2021;184:545-559 e22.
35. Feng Y, De Franceschi G, Kahraman A, et al. Global analysis of protein structural changes in complex proteomes. Nat Biotechnol 2014;32:1036-44.
36. Piazza I, Kochanowski K, Cappelletti V, et al. A Map of Protein-Metabolite Interactions Reveals Principles of Chemical Communication. Cell 2018;172:358-372 e23.
37. Holfeld A, Schuster D, Sesterhenn F, et al. Systematic identification of structure-specific protein–protein interactions. bioRxiv 2023:2023.02.01.522707.
38. Fernandes-Alnemri T, Wu J, Yu JW, et al. The pyroptosome: a supramolecular assembly of ASC dimers mediating inflammatory cell death via caspase-1 activation. Cell Death Differ 2007;14:1590-604.
39. Srinivasula SM, Poyet JL, Razmara M, et al. The PYRIN-CARD protein ASC is an activating adaptor for caspase-1. J Biol Chem 2002;277:21119-22.
40. Eisenbarth SC, Colegio OR, O'Connor W, et al. Crucial role for the Nalp3 inflammasome in the immunostimulatory properties of aluminium adjuvants. Nature 2008;453:1122-6.
41. Gabay C, Kushner I. Acute-phase proteins and other systemic responses to inflammation. N Engl J Med 1999;340:448-54.
42. Simons JP, Al-Shawi R, Ellmerich S, et al. Pathogenetic mechanisms of amyloid A amyloidosis. Proc Natl Acad Sci U S A 2013;110:16115-20.
43. Erdem E, Erdem D, Dilek M, et al. Red cell distribution width and mean platelet volume in amyloidosis. Clin Appl Thromb Hemost 2014;20:334-7.
44. Bakan A, Oral A, Alışır Ecder S, et al. Assessment of Mean Platelet Volume in Patients with AA Amyloidosis and AA Amyloidosis Secondary to Familial Mediterranean Fever: A Retrospective Chart - Review Study. Med Sci Monit 2019;25:3854-3859.
45. Rolfes V, Ribeiro LS, Hawwari I, et al. Platelets Fuel the Inflammasome Activation of Innate Immune Cells. Cell Rep 2020;31:107615.
46. Sponarova J, Nyström SN, Westermark GT. AA-amyloidosis can be transferred by peripheral blood monocytes. PLoS One 2008;3:e3308.
47. Couturier J, Stancu IC, Schakman O, et al. Activation of phagocytic activity in astrocytes by reduced expression of the inflammasome component ASC and its implication in a mouse model of Alzheimer disease. J Neuroinflammation 2016;13:20.
48. Pandey A, Shen C, Feng S, et al. Cell biology of inflammasome activation. Trends Cell Biol 2021;31:924-939.
49. Schenk D. Amyloid-beta immunotherapy for Alzheimer's disease: the end of the beginning. Nat Rev Neurosci 2002;3:824-8.
50. Senatore A, Frontzek K, Emmenegger M, et al. Protective anti-prion antibodies in human immunoglobulin repertoires. EMBO Mol Med 2020;12:e12739.
51. Sevigny J, Chiao P, Bussiere T, et al. The antibody aducanumab reduces Abeta plaques in Alzheimer's disease. Nature 2016;537:50-6.
52. Sonati T, Reimann RR, Falsig J, et al. The toxicity of antiprion antibodies is mediated by the flexible tail of the prion protein. Nature 2013;501:102-6.
53. Emmenegger M, De Cecco E, Lamparter D, et al. Continuous population-level monitoring of SARS-CoV-2 seroprevalence in a large European metropolitan region. iScience 2023;26:105928.
54. Lamparter D, Jacquat RPB, Riou J, et al. Code repository for SARS-CoV-2 seroprevalence study. 1.0.0 ed, 2022.
55. Mariathasan S, Newton K, Monack DM, et al. Differential activation of the inflammasome by caspase-1 adaptors ASC and Ipaf. Nature 2004;430:213-8.
56. de Alba E. Structure, interactions and self-assembly of ASC-dependent inflammasomes. Arch Biochem Biophys 2019;670:15-31.

57. Vajjhala PR, Mirams RE, Hill JM. Multiple binding sites on the pyrin domain of ASC protein allow self-association and interaction with NLRP3 protein. J Biol Chem 2012;287:41732-43.
58. Oroz J, Barrera-Vilarmau S, Alfonso C, et al. ASC Pyrin Domain Self-associates and Binds NLRP3 Protein Using Equivalent Binding Interfaces. J Biol Chem 2016;291:19487-501.
59. Vahdat Shariat Panahi A, Hultman P, Öllinger K, et al. Lipid membranes accelerate amyloid formation in the mouse model of AA amyloidosis. Amyloid 2019;26:34-44.
60. Richards DB, Cookson LM, Barton SV, et al. Repeat doses of antibody to serum amyloid P component clear amyloid deposits in patients with systemic amyloidosis. Sci Transl Med 2018;10.
61. Claus S, Meinhardt K, Aumuller T, et al. Cellular mechanism of fibril formation from serum amyloid A1 protein. EMBO Rep 2017;18:1352-1366.
62. Rocken C, Kisilevsky R. Comparison of the binding and endocytosis of high-density lipoprotein from healthy (HDL) and inflamed (HDL(SAA)) donors by murine macrophages of four different mouse strains. Virchows Arch 1998;432:547-55.
63. Moretti J, Blander JM. Increasing complexity of NLRP3 inflammasome regulation. J Leukoc Biol 2021;109:561-571.
64. Bodin K, Ellmerich S, Kahan MC, et al. Antibodies to human serum amyloid P component eliminate visceral amyloid deposits. Nature 2010;468:93-7.
65. Lundmark K, Westermark GT, Nystrom S, et al. Transmissibility of systemic amyloidosis by a prion-like mechanism. Proc Natl Acad Sci U S A 2002;99:6979-84.
66. Nilsson KP, Ikenberg K, Aslund A, et al. Structural typing of systemic amyloidoses by luminescent-conjugated polymer spectroscopy. Am J Pathol 2010;176:563-74.
67. Sjolander D, Rocken C, Westermark P, et al. Establishing the fluorescent amyloid ligand h-FTAA for studying human tissues with systemic and localized amyloid. Amyloid 2016;23:98-108.
68. Wahlström N, Edlund U, Pavia H, et al. Cellulose from the green macroalgae Ulva lactuca: isolation, characterization, optotracing, and production of cellulose nanofibrils.
69. Martín-Sánchez F, Gómez AI, Pelegrín P. Isolation of Particles of Recombinant ASC and NLRP3. Bio Protoc 2015;5.
70. Meisl G, Kirkegaard JB, Arosio P, et al. Molecular mechanisms of protein aggregation from global fitting of kinetic models. Nat Protoc 2016;11:252-72.
71. Yanagita T, Murata Y, Tanaka D, et al. Anti-SIRP. JCI Insight 2017;2:e89140.
72. Ono Y, Nagai M, Yoshino O, et al. CD11c+ M1-like macrophages (MΦs) but not CD206+ M2-like MΦ are involved in folliculogenesis in mice ovary. Sci Rep 2018;8:8171.
73. Arlt A, von Bonin F, Rehberg T, et al. High CD206 levels in Hodgkin lymphoma-educated macrophages are linked to matrix-remodeling and lymphoma dissemination. Mol Oncol 2020;14:571-589.
74. Nawaz A, Aminuddin A, Kado T, et al. CD206. Nat Commun 2017;8:286.
75. Emmenegger M, Kumar SS, Emmenegger V, et al. Anti-prothrombin autoantibodies enriched after infection with SARS-CoV-2 and influenced by strength of antibody response against SARS-CoV-2 proteins. PLoS Pathog 2021;17:e1010118.
76. Emmenegger M, Fiedler S, Brugger SD, et al. Both COVID-19 infection and vaccination induce high-affinity cross-clade responses to SARS-CoV-2 variants. iScience 2022;25:104766.
77. Emmenegger M, De Cecco E, Hruska-Plochan M, et al. LAG3 is not expressed in human and murine neurons and does not modulate alpha-synucleinopathies. EMBO Mol Med 2021;13:e14745.
78. Jagusiak A, Rybarska J, Konieczny L, et al. Amyloids, Congo red and the apple-green effect. Acta Biochim Pol 2019;66:39-46.